IEEE Access
Multidisciplinary ⋮ Rapid Review ⋮ Open Access Journal

Received 5 March 2024, accepted 8 May 2024, date of publication 9 May 2024, date of current version 17 May 2024.

Digital Object Identifier 10.1109/ACCESS.2024.3399709

APPLIED RESEARCH

Optimized Design of Multi-Channel Resonant Converter for Fuel Cell Application

DENYS IGOROVYCH ZAIKIN[1], (Member, IEEE), MARTIN KOLDING ANDERSEN[1], MARK BRIX RUGTVED RUGHOLT[1], THOMAS KRAG KJELDSEN[1], AND POOYA DAVARI[2], (Senior Member, IEEE)

[1]Advent Technologies A/S, 9000 Aalborg, Denmark
[2]Department of Energy, Aalborg University, 9220 Aalborg, Denmark

Corresponding author: Denys Igorovych Zaikin (Denys.Zaikin@advent.energy)

This work was supported by the Det Energiteknologiske Udviklings- og Demonstrationsprogram [Energy Technology Development and Demonstration Program (EUDP)]-Danish Energy Agency through the Project "Marine Fuel Cell Auxiliary Power Unit" under Grant 64020-2072.

ABSTRACT This research presents a multi-channel phase shift inductor-inductor-capacitor (LLC) resonant converter with a wide input and output voltage range that has been specially optimized for fuel cell applications. The worst-case minimum stack voltage and the battery voltage range were used to determine the optimal parameters of the LLC converter. The voltage gain of the converter operating at a constant power was considered, and an algorithm for such a calculation is proposed. Current balancing is implemented using channel temperature measurements, circumventing the need for expensive current sensors. A natural self-balancing mechanism is investigated for converters operating at high frequencies exceeding the series resonance frequency of a resonant converter. Efficiency optimization recommendations for the transformer turn ratio of the converter are illustrated. Multi-object optimization is implemented to achieve an optimized design so that both the minimum and maximum voltage gains can be realized; simultaneously, the transformer turn ratio is kept at a minimum to maintain high efficiency. An experimental prototype of a four-channel converter is implemented and verified at a 5-kW power level. Active content and the C language code files for converter calculations are also provided in this paper.

INDEX TERMS Current sharing, fuel-cell converter, multi-objective optimization, resonant converter.

I. INTRODUCTION

Fuel cell applications have seen tremendous widespread adoption in recent years. Fuel cell technology allows for reduced emissions in some critical applications. Methanol, hydrogen, and other substances can be used to produce electricity via fuel cell technology. The proposed converter is intended to operate in a methanol fuel cell unit [1], [2]. In marine applications, fuel cell systems allow for significant emission reductions. For example, some city ports require emission-free profiles for ships seeking to dock. Certain small boats can be powered solely by fuel cell units [3], which facilitates highly autonomous operation without the need to recharge batteries. Another important application is telecom backup power systems [4], [5]. Fuel cell backup power systems allow telecom installations to operate in almost completely isolated locations. In the automotive industry, fuel cell systems are used in emission-free vehicles–typically buses and cars–and as a backup solution [6]. In summary, fuel cells can be a replacement for fossil fuel power generation, e.g., diesel generators, where an emission-free operation and the absence of audible noise are required. Thus, it is apparent that the following parameters are crucial for fuel cell applications: high efficiency across a very wide range of input/output voltages. To comply with regulations and satisfy the conditions for approval, strict electromagnetic compatibility (EMC) requirements must also be met. Consequently, there are a lot of constraints to implementing power electronics and converters in fuel cell applications.

The associate editor coordinating the review of this manuscript and approving it for publication was Fengjiang Wu.

© 2024 The Authors. This work is licensed under a Creative Commons Attribution 4.0 License.
For more information, see https://creativecommons.org/licenses/by/4.0/

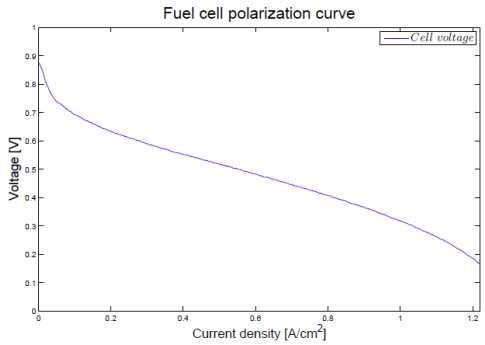

FIGURE 1. Typical polarization V-I curve for a methanol fuel cell (single-cell voltage). Source: [1].

Fuel cell systems have the following characteristics:

1) Fuel cells feature a high output voltage range. An example of the typical voltage-current characteristics of a methanol fuel cell is presented in Fig. 1 [1]. In addition, the loaded stack voltage changes during the life of the stack. Hence, the voltage can change more than twice during fuel cell operation.
2) The typical load for a fuel cell system converter is a battery or supercapacitor. Batteries are typically used in the telecommunications industry, and supercapacitors provide DC link energy storage in automotive and marine applications.
3) High efficiency is required for a full fuel cell system to yield commercial benefits. Thus, for a wide range of input and output voltages, the DC-DC converter in the fuel cell must have an efficiency of more than 95%.
4) Galvanic isolation is a mandatory safety requirement for automotive or domestic applications.

The features required in the next generation of DC-DC converters for fuel cell systems can be specified as follows:

- Wide input/output voltage range
- High efficiency
- Low volume and compact size to meet market requirements
- Ability to operate with a battery-like load (i.e., with the voltage source at the output)
- Constant power load behavior, which can be caused by either a fixed fuel cell voltage-current set point or the customer-side system consuming a fixed amount of power.

DC-DC converter typologies for fuel cell applications have been proposed extensively in the literatures [7], [8], [9], and [10]. Current fed isolated converters ([7], [8]) have low robustness and low efficiency or complex switching control. Because the fuel cell source voltage can change by as much as a time factor of two, two-stage converters are conventionally employed in such applications [10], impairing system efficiency with the increased number of components.

To meet the criteria mentioned earlier, two topologies were considered. One is the phase shift full-bridge converter (PSFB) [9], and the second is the inductor-inductor-capacitor (LLC) resonant converter [11]. The PSFB converter has too many components and snubbers to achieve high efficiency, while the conventional LLC converter is limited in its input and output voltage ranges. Comparisons of both typologies can be found in previous studies [12], [13]. Because the LLC converter has excellent advantages in achieving EMC, low volume, and a small number of components, this converter family was chosen as the base converter for the fuel cell module.

The conventional LLC converter uses pulse frequency modulation, the switching bridge generates a square waveform to excite the LLC resonant tank. However, the major drawback of the conventional LLC converter is the limited range of its input-output voltage ratio [11], [12]. To overcome these limitations, a number of studies have focused on improving the features of this converter using different techniques [14], [15], [16], [17], [18], [19], [20], [21], [22], [23], [24], [25], [26]. Certain studies [14], [24] propose additional switches and implement a multilevel structure to improve the features of the converter when operated at a fixed switching frequency. Several other studies [15], [21], [23], [25] modify the resonant circuit, incorporating new elements to improve the transfer function of the resonant tank. One study [16] uses a variable inductor controlled via DC current to regulate the voltage ratio at different load levels. Interleaved converters with modified rectifiers and phase shift control were employed in [17]. Unsymmetrical control and modes for the bridge arm of the full-bridge converter were implemented to achieve a wide input voltage range in [18]. An adaptive turn ratio change in the transformer facilitated achieving a wide output voltage range in [19] and [26]. Additional bridge arm and secondary-side rectifier connections were used in the hybrid full-bridge and LLC converter in [20]. On-the-fly topology morphing of full-bridge and half-bridge operations is proposed in [22].

Instead of adding extra components, some researchers have focused their research on numerically optimizing the conventional LLC converter using computer-aided optimization design [27], [28]. However, these optimizations are applied to converters operating at a fixed or limited range of input and output voltages. In [27], the input voltage is fixed at 12 V and the output voltage is fixed at 400 V. In [28], the input voltage is limited to a 25-35 V range, and the output voltage is fixed at 400 V. Thus, the aforementioned approaches are not relevant to fuel cell applications in which a wide stack voltage range and a wide battery voltage range are required.

It is apparent that all the listed solutions are somewhat difficult to implement practically because these solutions either increase the number of components and, thus, the size of the converter, or the complex microcontroller-based control employed does not permit robust operation of the converter. Because of these limitations, the phase shift LLC (PSLLC) resonant converter has been chosen for the practical implementation of the fuel cell module [30], [31], [32], [33], [34].

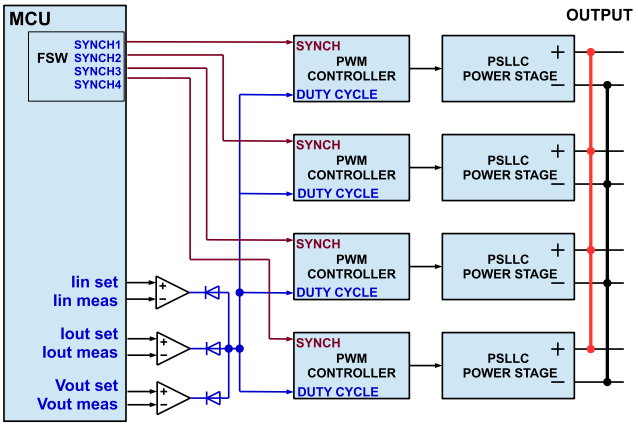

FIGURE 2. Microcontroller (MCU) and control circuit block diagram.

TABLE 1. Converter characteristics.

Input voltage range, V_{in}	$60\,V \ldots 120\,V$
Input nominal voltage, V_{in}^{nom}	$66.0\,V$
Output power (max), P_{out}	$5.6\,kW$
Maximum power (per channel), P_{out}^{max}	$1.4\,kW$
Maximum stack (input) current, I_{in}^{max}	$85.0\,A$
Output voltage range (per channel), V_{out}	$200\,V \ldots 300\,V$
Nominal output channel voltage V_{out}^{nom}	$250\,V$
Number of interleaved channels	4
Switching frequency range	$70 \ldots 170\,kHz$
L_r (includes external and leakage inductances)	$1.5\,\mu H$
C_r	$5 \times 220\,nF = 1.1\,\mu F$
L_m	$10.0\,\mu H$
$1:N$	1:4

The rest of this paper is structured as follows: Section II focuses on the features and structure of the DC-DC converter for fuel cell application, and converter control is examined in Section III. The voltage gain characteristics of the fuel cell LLC resonant converter operating in a constant power mode are presented in Section IV. The channel balance mechanisms, including channel temperature measurement and the self-balancing effect at high frequencies, are described in Section V. Efficiency optimization recommendations and an optimization algorithm are provided in Section VI. The experimental data are outlined in Section VII, and finally, conclusions are drawn in Section VIII.

II. CONVERTER STRUCTURE

A simplified block diagram of the entire multichannel converter proposed for fuel cell applications, along with its control circuit, is presented in Fig. 2. The technical parameters of the converter are listed in Table 1. The outputs of the converter channels are connected in parallel on the input and output sides. This configuration represents the worst-case setup from a channel current balancing perspective.

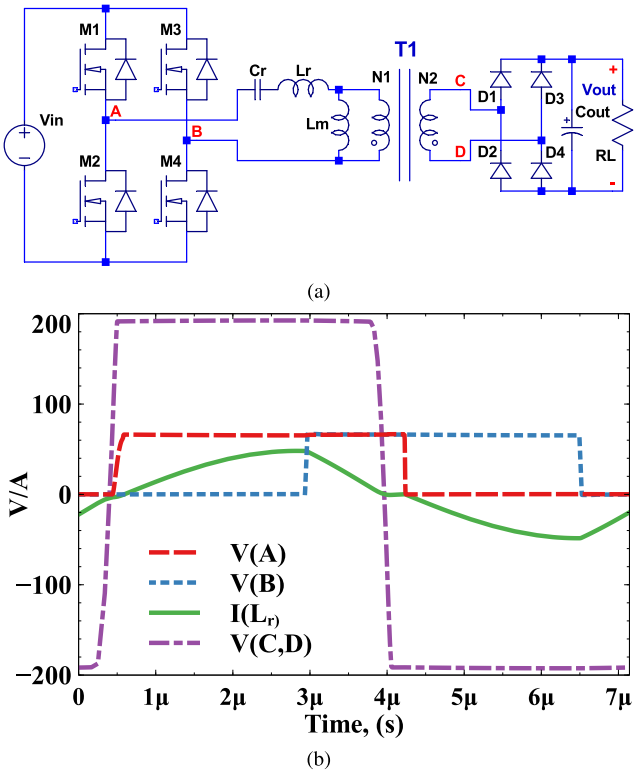

FIGURE 3. (a) Schematic and (b) waveforms of a channel of the PSLLC converter.

The converter contains four interleaved phase-shifted LLC resonant converter channels; a diagram and waveforms of one power channel are presented in Fig. 3. It represents a conventional full-bridge LLC resonant converter with phase shift implemented.

III. CONVERTER CONTROL

The proposed fuel cell power converter is designed to use batteries and different power consumers at its output. Thus, the mode of operation is close to a constant power mode; the features of this mode are examined in Section IV. As can be seen in Fig. 2, the interleaved converter is controlled by a microcontroller (MCU) that calculates the switching frequency in accordance with the algorithm presented subsequently. The MCU continually measures the input current, output current, and voltages used for the switching frequency calculation. The feedback control includes three loops that allow for control of the input current (stack current), the output current, and the output voltage, as shown in Fig. 2. Therefore, the MCU also has digital-to-analog converters (DAC) that set or limit the input and output currents and the output voltage. The converter values and control loops described earlier facilitate charging batteries on the output side in different charging modes, such as under a constant input or output current, output voltage, or power. In most cases, the primary control method involves adjusting the set point of the input stack current, which is the most critical

parameter of the system. The output power and voltage can be limited by regulating the input stack current alone.

Analog control loops are implemented to stabilize or limit one of the following parameters: input current, output current, or output voltage. If the switching frequency controller is already at its maximum limit and, concurrently, the DC gain of the converter is still high, the analog control loops regulate the phase shift between the full-bridge legs, reducing the equivalent duty cycle of the converter primary stage and the energy flowing to the secondary side. The controller for this additional control loop can be either analog or digital. In this study, an analog controller is implemented because there are many commercially available integrated circuits (IC) for full-bridge converters with phase shift. Examples of such ICs include UCC2875, UC2895, and LTC3722.

The main MCU continually controls the switching frequency via feed-forward calculation of the theoretical switching frequency. The algorithm endeavors to keep the switching frequency at the highest possible maximum value to operate as closely as possible to the conventional LLC converter mode by trying to keep the primary duty cycle as close to one as possible. In this case, the phase shift between the half-bridge legs will be close to 180°.

A specific procedure is employed to derive the control algorithm. To predict the switching frequency, the first-harmonic approximation (FHA) method is used [11] to calculate the DC voltage gain of the LLC converter. The converter's input and output currents and voltages are measured and recorded to calculate the switching frequency. Eq. (1) expresses the DC gain of a conventional LLC converter.

$$M_{dc} = \frac{V_{out}}{V_{in}} = \left| \frac{j\omega L_m N\, R_e}{(j\omega L_m + R_e)\left(\frac{j\omega L_m R_e}{j\omega L_m + R_e} + j\omega L_r + \frac{1}{j\omega C_r}\right)} \right|, \quad (1)$$

where L_m is the equivalent magnetizing inductance, L_r is the equivalent resonant inductance, and $N = N_2/N_1$ is the equivalent turn ratio of the transformer T1 (Fig. 3). The parameter L_r may also include the leakage inductance of transformer T1. Together with the resonant inductance, the aforementioned three parameters of the transformer and can be considered a full equivalent model of the transformer and can be derived from measurements of transformer parameters [47]. The parameter R_e represents the equivalent load resistance reflected to the primary side [11]. It can be calculated from the converter load resistance R_L, as follows:

$$R_e = \frac{8}{\pi^2}\frac{1}{N^2}R_L. \quad (2)$$

The angular frequency ω in Eq. (1) is determined as $\omega = 2\pi F_{sw}$, where F_{sw} is the switching frequency that must be calculated and set by the MCU.

The simplified algorithm for the switching frequency calculation can be developed as follows:

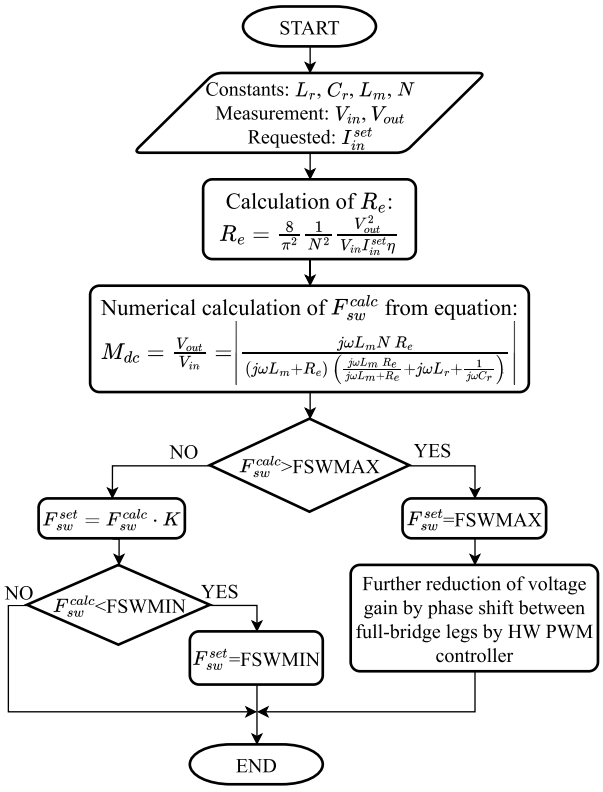

FIGURE 4. Flow chart diagram of the algorithm for calculating the switching frequency of the converter.

- Constant parameters L_r, L_m, N and C_r are defined.
- Parameter M_{dc} is indirectly measured and calculated from input and output voltage measurements.
- Parameter R_e is calculated and measured using the required input current set point I_{in}^{set} instead of the measured stack current at the moment I_{in}. With this approach, feed-forward control of the switching frequency is performed. Here, it is assumed that the main control of the converter is performed by setting and controlling the stack (input current). Output current and output voltage are also controlled, but are set to maximum safe levels to avoid over-current and over-voltage of the battery. Consequently, the parameter R_e can be calculated using Eq. 2, as follows:

$$R_e = \frac{8}{\pi^2}\frac{1}{N^2}\frac{V_{out}^2}{V_{in}I_{in}^{set}\eta}, \quad (3)$$

  where η is the expected efficiency of the converter (for example, $\eta = 0.95$).
- Eq. (1) is solved numerically using the bisection method for the variable ω, and finally, the calculated switching frequency F_{sw}^{calc} is calculated.

The algorithm for calculating and setting the feed-forward switching frequency F_{sw}^{set} is diagrammed in Fig. 4. As can be seen, if the calculated switching frequency falls within a permitted range of frequencies: F_{sw}^{min} to F_{sw}^{max}, the final switching frequency for the converter is adjusted using a

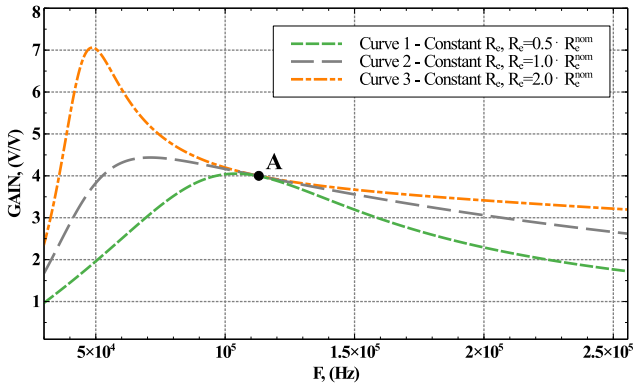

FIGURE 5. Transfer characteristics of the proposed LLC converter calculated for different load resistances R_e.

coefficient $K = 0.8 \ldots 1.0$, which takes into account the tolerances and accuracy of the components of the converter.

$$F_{sw}^{set} = F_{sw}^{calc} \cdot K \tag{4}$$

This coefficient can also be used to take into account the difference between the theoretically calculated voltage gain and the realistic one, as described in Section VII.

IV. FUEL CELL LLC RESONANT CONVERTER WORKING IN CONSTANT POWER MODE

This section deals with an issue that is linked to the conventional approach used in most research touching on the theoretical calculation of LLC DC gain [11], [12], [34]. The conventional approach is exemplified by Eq. (1), which can be used to calculate the DC gain characteristics of the LLC converter, depending on the switching frequency. However, the main issue here, using such a direct approach, is that Eqs. (1) and (2) use a constant resistance as the load R_L or parameter R_e, directly assuming that the converter operates with a constant resistance at the output. The typical transfer characteristics of the LLC converter calculated using Eq. (1) are illustrated in Fig. 5.

The controller for the primary system requests the current level of the stack, thus power from the stack can be considered a constant at any current moment in time, along with the input (stack) voltage. This means that the converter output also operates in a constant power mode on the input and output sides. At the same power level, the output voltage of the converter can vary in a wide range, depending on the battery charge level and the operation of the entire system operation. The required range of output voltages for the entire system can be as wide as ±20% or higher.

It is assumed that the converter operates with constant input values and that the gain level corresponds to Point A in Fig. 5. At the nominal (maximum) power level, the converter is loaded with equivalent resistance at the output R_e^{nom}, which is calculated for the nominal output battery voltage V_{out}^{nom}. Thus, the gain characteristics of the converter at this moment correspond to Curve 2 in Fig. 5. At some moment in time, the battery level reduces and the voltage on the converter's output also reduces, but the power generated by the fuel cell remains the same and constant. The converter controller increases the switching frequency to reduce the converter's gain to match the new battery voltage level. This means that with the same power and a reduced voltage at the output, the load resistance R_L and, therefore, R_e also decrease. It is not possible, at this moment, to calculate the transfer characteristics and voltage gain using Curve 2 in Fig. 5. The real characteristics of the gain will lie somewhere between Curve 1 and Curve 2 to the right of Point A.

A similar process occurs when the battery voltage increases. The converter controller decreases the switching frequency to increase the converter's gain to match the new battery voltage level. This means that with the same power at the output and an increased output voltage, the load resistance R_L and, therefore, R_e are also increased. The real characteristics of the gain will lie somewhere between Curve 3 and Curve 2 on the left from Point A.

Notably, this situation is not a problem for the converter control diagrammed in Fig. 4. The algorithm will keep switching the frequency, knowing all the needed parameters, such as the input and output voltages and the input currents.

The corrected voltage gain characteristics are necessary for a proper estimation of the possibility of the LLC converter providing operation at full input and output voltage levels. The static characteristics presented in Fig. 5 for fixed load resistance cannot be used directly. The characteristics of the converter are impacted by the dynamic changes in parameter R_e when the output voltage changes; however, the power level remains constant. For each frequency, the R_e resistance and the voltage gain M_{dc} should be calculated using the numerical iterative method, in which the current value of the parameter R_e is used to estimate the value of the new voltage gain using Eq. (1). The new voltage gain, along with the input voltage and output power, will then determine the new value of the parameter R_e. The process is continuous until R_e does not change from iteration to iteration.

The corrected voltage gain will now also depend on the input voltage V_{in} because the converter is driven from the stack and power transfers from the stack to the battery. The lower the input stack voltage at a constant power level, the lower the output voltage; thus, the load resistance R_e decreases, impacting the resulting voltage gain.

The algorithm of the corrected voltage gain numerical calculation is diagrammed in Fig. 6. This algorithm is not employed in the control of the converter but allows for predicting and calculating the possibilities of the LLC converter delivering the required level of power to the load. The parameter R_e^{nom} is defined as the equivalent load resistance at nominal conditions at the output at nominal battery voltage V_{out}^{nom} and nominal (maximum) output power P_{out}^{max}.

$$R_e = \frac{8}{\pi^2} \frac{1}{N^2} \frac{(V_{out}^{nom})^2}{P_{out}^{max}} \tag{5}$$

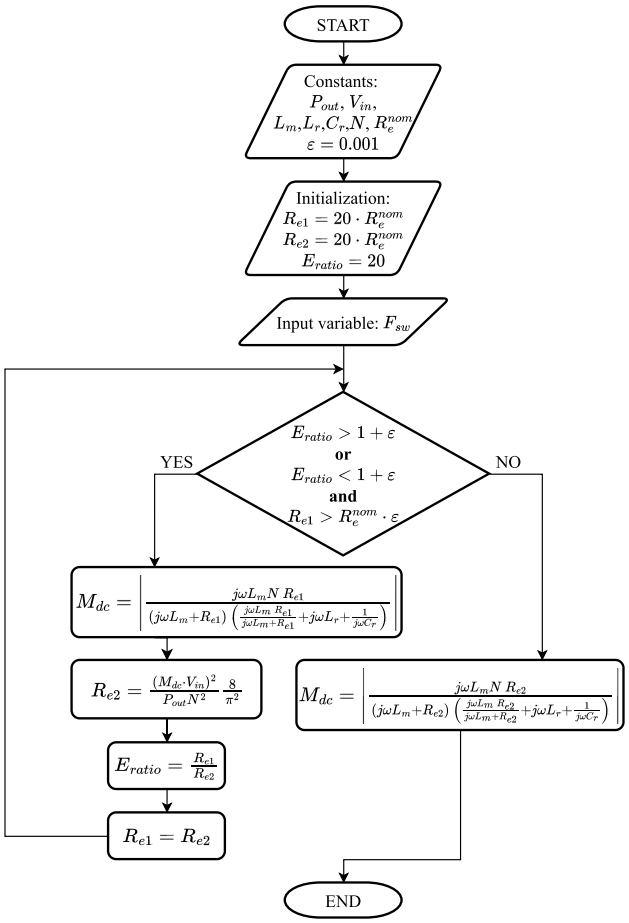

FIGURE 6. Flow chart diagram of the algorithm for calculating the voltage gain of an LLC converter operating at constant power.

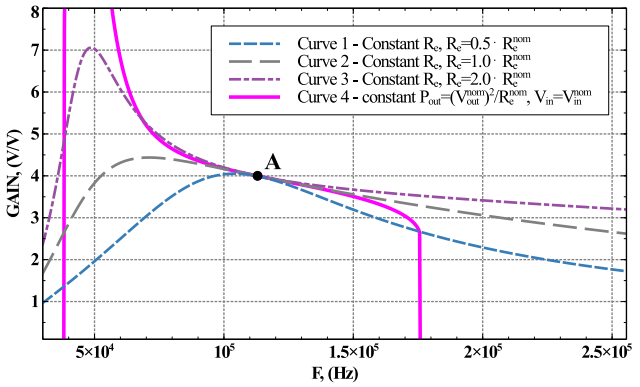

FIGURE 7. Transfer characteristics comparison for a calculation using the constant R_e (Eq. (1)) and corrected for constant power (Fig. 6).

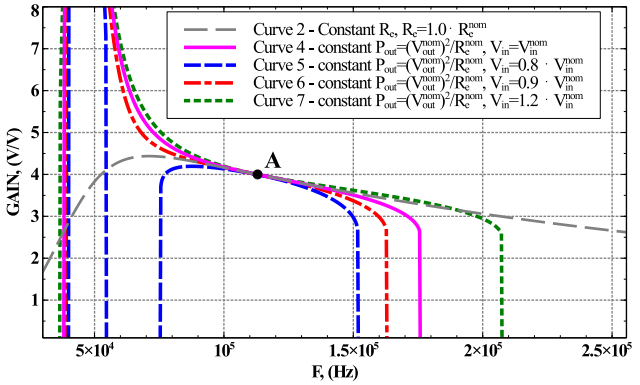

FIGURE 8. Transfer characteristics comparison for a calculation using the constant R_e (Eq. (1)) and corrected for constant power (Fig. 6), illustrating the effect of input voltage V_{in} at constant power.

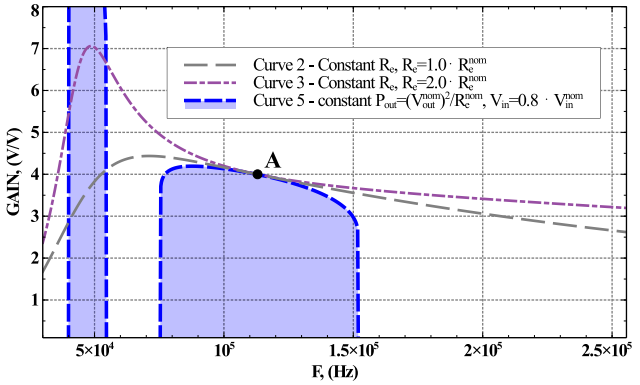

FIGURE 9. Transfer characteristics comparison for a calculation using the constant R_e (Eq. (1)) and corrected for constant power (Fig. 6), illustrating the effect of a low input voltage V_{in} at constant power.

In the iterative process, the parameter R_e^{nom} is used in the algorithm as a reference for defining the initial values of the equivalent resistances $R_{e1} = 20 \cdot R_e^{nom}$ and $R_{e2} = 20 \cdot R_e^{nom}$. The parameter $\varepsilon \ll 1$ determines the criteria for the iterative algorithm to stop iterations with some accuracy when the equivalent resistance is at steady state.

An example of the voltage gain characteristics is presented in Fig. 7. As can be seen, Curve 4 is calculated for constant power, and in comparison to Curve 2, it behaves as described earlier.

The effect of the level of the input voltage is shown in Figs. 8 and 9.

On analyzing Figs. 7–9, several facts are noteworthy.

The switching frequency of the converter operating at constant power will place some limits on the power that can be achieved at certain input stack voltages. Above certain maximum and minimum switching frequencies, which depend on the input voltage and the output power, the voltage gain drops rapidly and theoretically decreases to close to zero. This can be explained by the fact that with the same power and a reduced voltage at the output, the load resistance R_L and, therefore, R_e, also decrease. A reduction in the load resistance will cause a reduction in the voltage gain and the output voltage (Fig. 7), and the drop in the voltage will lower the load resistance further at constant power, and so on. Thus, the process will become avalanche-like, and the load resistance and voltage gain will rapidly drop to zero.

The effect of the input stack voltage is also evident, especially in cases where the input voltage drops below a certain limit: the voltage gain characteristics will include breaks and regions where the gain is zero (Figs. 8 and 9). The reason for this effect is similar to that described earlier, except

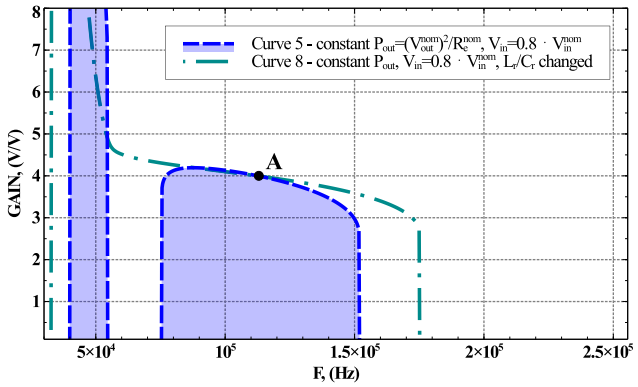

FIGURE 10. Effect of changing L_r and C_r on the voltage gain characteristic calculated for constant power.

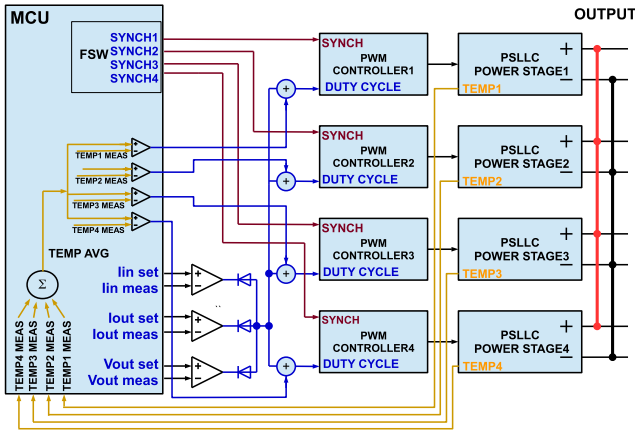

FIGURE 11. Converter control circuit block diagram demonstrating current balancing via power channel temperature measurement.

that the output voltage drops further as the input voltage decreases. If the calculation by the algorithm diagrammed in Fig. 6 exhibits breaks in the voltage gain, the design of the LLC converter should be corrected; for example, by changing the values of L_r and C_r in the same way, the quality factor $Q_{rr} = \sqrt{\frac{L_r}{Cr}}/R_e$ is reduced by 1.5 times while maintaining the same series resonance frequency $F_{rr} = \frac{1}{2\pi}\frac{1}{\sqrt{L_r C_r}}$. The result of the correction of the converter design is presented in Fig. 10.

Typically, for practical calculation of the fuel cell LLC resonant converter with phase shift, the voltage gain calculation presented earlier should be performed for the maximum operating output power and the lowest possible minimum input voltage. The input stack voltage may be specified at the end of life of the fuel cell stack as a worst-case scenario in which the stack voltage is diminished in comparison to the new stack voltage. The excess voltage gain at higher input voltages will be compensated for by operating at a higher switching frequency and an additional phase shift between the full-bridge legs.

As can be seen from Figs. 7–10, in a constant power mode, the converter generates a significant increase in the voltage gain within the low-frequency range around the pole frequency $F_{rm} = \frac{1}{2\pi}\frac{1}{\sqrt{(L_r+L_m)C_r}}$. As explained earlier, the rapid increase in gain can be explained by the high equivalent load resistance R_e at high output voltages and constant power. This behavior at low frequencies can be used to design a converter that meets a wide range of output and input voltage requirements. The only drawback to operating at frequencies much lower than the series resonant frequency F_{rr} is the risk of losing zero voltage switching (ZVS) for primary switches and, thus, increased switching losses.

V. CURRENT BALANCING METHODS

A. METHOD 1 – CURRENT BALANCING USING CHANNEL TEMPERATURE

Power channels in an interleaved multichannel converter need to be balanced to conduct the same current or power to the load [36], [37], [38], [39], [40], [41], [42], [43], [44], [45], [46]. Thus, a balancing technique is required for converter robustness and a long life span. The worst case here is when the channels are configured to be connected in parallel on the primary and secondary sides.

Because the stack current typically cannot increase very quickly, channel current balancing can be implemented using a method in which the temperature of each channel is measured instead of the current. This approach is illustrated in Fig. 11. A temperature sensor is placed close to one of the power switches in each channel and monitored by the MCU. The average temperature is calculated, and the temperature of the channel is compared with the average temperature. A correction to the duty cycle is then applied by the MCU in such a way as to compensate for the difference between the channel temperature and the average temperature.

The advantages of this method of channel balancing are its simple design and small number of components. There is no need for current sensing in each channel; thus, the same input DC link net—connected directly to the stack and all the channels—can be used. This improves current sharing between bypass capacitors on the input side of an interleaved multichannel converter.

The disadvantage of thermal channel balancing is its slow response characteristics. Furthermore, the channels of the converter cannot be identical in geometry and cooling conditions; hence, there may be some error in channel current balancing because of the differing temperatures of the channels.

B. METHOD 2 – CURRENT BALANCING USING A SELF-BALANCING MECHANISM

With the voltage gain characteristics of an LLC resonant converter operating in a constant power mode, as described in Section IV, it is possible to explore the effect of current imbalance in the channels. Let us consider two channels that are connected in parallel on the primary and secondary sides. Now, it is assumed that one of the channels has a higher output power for some reason, and the other parameters

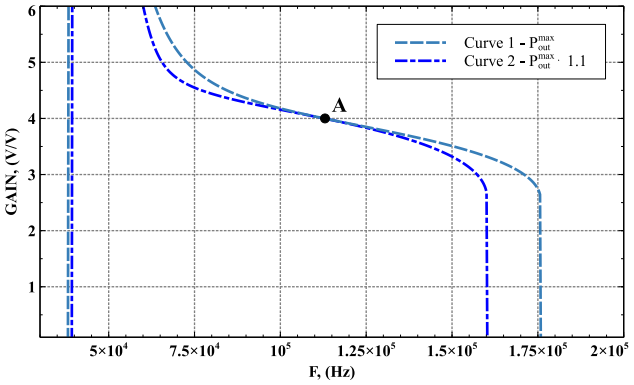

FIGURE 12. Effects of increasing the output power of one of the channels on the voltage gain characteristics of the resonant converter.

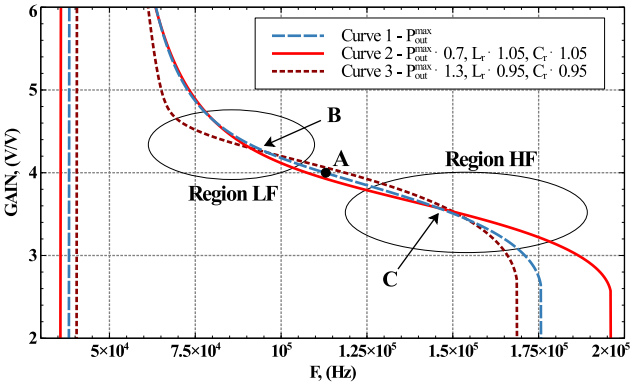

FIGURE 13. Effects of changing the output power of one of the channels on the voltage gain characteristics of the resonant converter when additional resonant circuit parameters have some tolerance or distribution around nominal values.

of the circuit are the same. A comparison of such channel characteristics is presented in Fig. 12. It can be seen that there is a reduction in gain when the switching frequency is moving from the series resonant frequency F_{rr} (Point A) to the left or right. This means that, at least at these frequencies, there is some self-balancing mechanism of current balancing between channels. This mechanism will not balance the channels fully because it is not based on feedback regulation but only on natural gain reduction when power is increased in one channel and decreased in another.

Furthermore, Fig. 13 illustrates the power imbalance effect on voltage gain due to converter element tolerance, where some displacement from the nominal parameters L_r and C_r in a resonant circuit is implemented. Fig. 13 further proves that moving from Point A to the right, there tends to be less difference in the voltage gain than at Point A directly. Therefore, the channel with the higher power and voltage gain (Curve 3 in Fig. 13) will lower the output power in the high frequency (HF) region, and in the opposite direction, the channel with the lower power and voltage gain (Curve 2 Fig. 13) will increase the output power in the HF region. This mechanism reduces the difference in the strength of the currents in the channels to some degree. The expected range of frequencies in which such a self-balancing mechanism is expected to be effective is approximately Point A to Point C in Fig. 13.

The natural current balancing mechanism described can be especially useful at high frequencies (HF region) because, in this region, it is critical to have effective channel balancing on account of the expected efficiency reduction at high frequencies.

It should be noted that in low frequency (LF) region, the self-balancing mechanism might fail. As can be seen from Fig. 13, in the LF region, the total voltage gain decreases when the switching frequency is increased. However, the difference in the gain increases simultaneously, which can cause some instability or failure in channel balancing. In conclusion, the self-balancing algorithm is most effective in the frequency range higher than the series resonant frequency F_{rr} (Point A). When the switching frequency increases beyond Point C, there is the same tendency for the channel balancing to fail due to the difference in the gain beyond Point C. Thus, the proposed self-balancing method may be useful for an LLC converter intended to operate on frequencies higher than the series resonant frequency F_{rr}.

Considering the foregoing reasoning, the algorithm for the switching frequency calculation and control diagrammed in Fig. 4 can be replaced with an algorithm that monitors the stack current and adapts the frequency to keep this current equal to the required value, as illustrated in Fig. 14. This algorithm endeavors to keep the switching frequency as high as possible so that the measured stack current matches the required value. Thus, the switching frequency is no longer feed-forward calculated but is controlled digitally, similar to the switching frequency of a conventional LLC converter. The MCU changes the frequency back and forth in small steps ΔF to keep the input current steady. The small change in frequency in each iteration corresponds to the integrator stage in the feedback control loop. The drawback of this algorithm is that, due to the digital implementation of feedback control and discretization of the frequency, there are some ripples in the stack current. The advantage of this algorithm is that it is much simpler than the one in Fig. 4 and uses less MCU resources. Generally, the algorithm diagrammed in Fig. 14 can be used as an alternative to the algorithm diagrammed in Fig. 4 if some ripples in the stack current are acceptable.

The natural current balancing mechanism in an LLC resonant converter working in a constant power mode, as described here, may be explored further in future research.

VI. EFFICIENCY OPTIMIZATION AND DESIGN PROCEDURE FOR A RESONANT CONVERTER FOR A FUEL CELL SYSTEM

A. TURN RATIO EFFECT ON EFFICIENCY

It can be shown that the root-mean-square (RMS) current of the secondary-side switches can be expressed as follows [48]:

$$I_{RMS}^{sec} \approx \frac{P_{out}}{V_{out}} \frac{\pi}{2\sqrt{2}}. \tag{6}$$

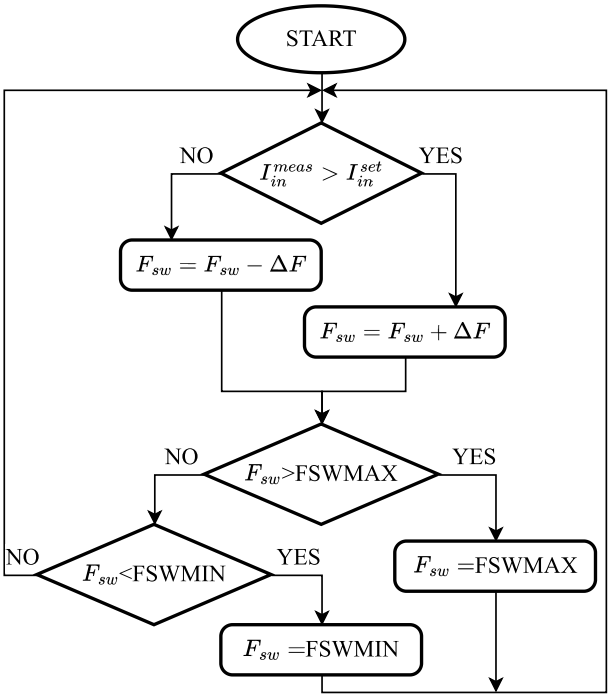

FIGURE 14. Algorithm for channel balancing via switching frequency control in regions HF and LF in Fig. 13.

Thus, the primary side switch RMS current can be expressed as follows [48]:

$$I_{RMS}^{pri} \approx \frac{P_{out}}{V_{out}} \frac{\pi}{2\sqrt{2}} \cdot N. \tag{7}$$

Eq. (7) is a simplified expression of the primary current that ignores the current component flowing in the magnetizing inductance. For the full range of operating switching frequencies, it is impossible to derive the full equation that includes this current component; however, some approximations can be found in [28], [55], and [61]. In our study, it is assumed that the magnetizing current is smaller than the reflected secondary-side transformer current. Thus, Eq.(7) is a good approximation for the primary RMS current. It can be assumed that the conduction losses on the primary side are directly dependent on the RMS current in the primary switches:

$$P_{cond}^{pri} = 2 \cdot {I_{RMS}^{pri}}^2 \cdot R_{DCon}. \tag{8}$$

Analyzing Eqs. (6)–(8), it is apparent that the only primary RMS current may be reduced during the LLC converter optimization process, and the only way to increase efficiency is to decrease the parameter N. Thus, the target of efficiency improvement is to decrease the parameter N to its lowest possible minimum value. However, because the parameter N also determines the voltage gain characteristics expressed as Eq. (1), a lack of gain must be compensated for using the rapid gain increase in the low-frequency range of the LLC converter operating in constant power mode, as illustrated in Figs. 7 and 10.

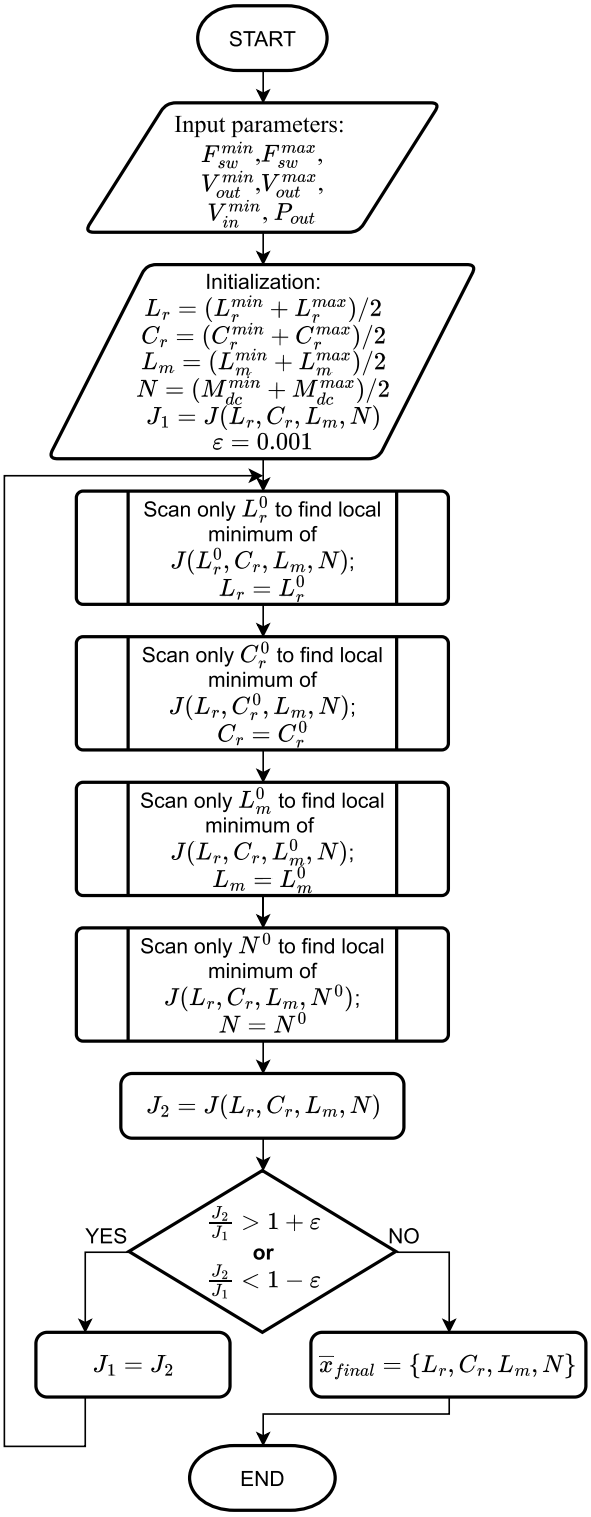

FIGURE 15. Algorithm for utilizing multi-objective optimization for efficiency optimization in the proposed LLC converter design.

B. MULTI-OBJECT OPTIMIZATION OF THE LLC CONVERTER

Optimization methods and approaches and their main characteristics are presented in Table 5 in the appendix section—the literature overview is summarized in this table. The

referenced studies use different techniques and intermediate objectives to achieve the optimal design of an LLC converter. The most critical parameters compared in Table 5 are as follows: objective function, design variables, input-output voltage ranges, and how the calculation method handles the constant power mode. Most studies research LLC converters that operate with a limited voltage range on the output side. If the LLC converter is designed to operate at a fixed output voltage, the load resistance is also fixed and is used as a constant load resistance for the gain characteristic calculation. For the proposed fuel cell application—with wide input and output voltages—a constant load resistance cannot be used for the gain calculation because this resistance changes with the output voltage in constant power mode.

Considering the foregoing reasoning, the procedure used to optimize the converter design and achieve the high efficiency of a phase-shifted resonant converter is illustrated in Fig. 15. This procedure represents multi-objective optimization (MOO) using a weighted sum method with normalization. Normalization can be done in relation to user-defined minimum and maximum levels of acceptance for each objective. These user-defined minimum and maximum parameters are called Utopia and Nadir points, respectively [62]. Multi-objective optimization is performed using multivariable function minimization. Multivariable function minimization is based on a simple search method that uses unit vectors as a set of search directions or as a method of single-parameter variation [62, p. 413], [63, Section 3.2].

Here, it is assumed that the input variable for the optimization algorithm is given by the vector $\overline{x} = \{L_r, C_r, L_m, N\}$. The objective function, the minimum of which must be found, can be expressed as follows:

$$J(\overline{x}) = w_1 \frac{|M_{dc}(\overline{x}, F_{sw}^{min}) - M_{dc}^{max}|}{M_{dc}^{max}} + w_2 \frac{|M_{dc}(\overline{x}, F_{sw}^{max}) - M_{dc}^{min}|}{M_{dc}^{min}} + w_3 \frac{N}{N^{(U)} - N^{(N)}}, \tag{9}$$

where M_{dc}^{min} and M_{dc}^{max} are the minimum and maximum voltage gains required from the converter specification; F_{sw}^{min} and F_{sw}^{max} are the specified minimum and maximum switching frequencies; the voltage gain M_{dc}^{min} is expected to be achieved at maximum frequency F_{sw}^{max}, and voltage gain M_{dc}^{max} is expected to be achieved at minimum frequency F_{sw}^{min}. For the phase-shifted LLC converter, the minimum and maximum gains can be specified as follows:

$$M_{dc}^{min} = \frac{V_{out}^{min}}{V_{in}^{min}}$$
$$M_{dc}^{max} = \frac{V_{out}^{max}}{V_{in}^{min}}, \tag{10}$$

where V_{in}^{min} is the minimum stack voltage at the maximum load current. Further reduction in the voltage gain at high input voltages is achieved by an equivalent gain reduction in the phase shift between the passive and active full-bridge legs, as described in Section III. The voltages V_{out}^{min} and V_{out}^{max} are specified as the minimum and maximum battery voltages.

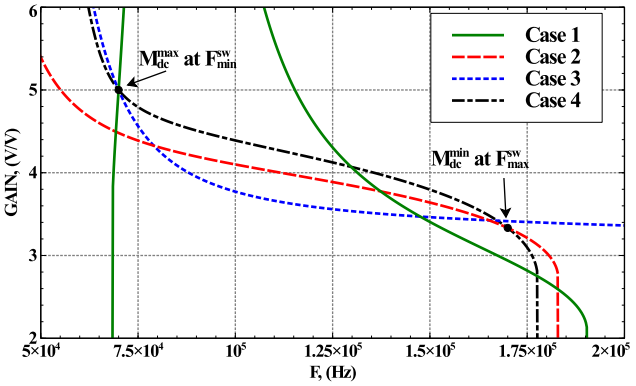

FIGURE 16. Results of multi-object optimization and their comparison for different input parameters. $V_{in}^{min} = 60.0\,V$, $V_{out}^{min} = 200\,V$, $V_{out}^{max} = 300\,V$, $P_{out} = 1375$, $F_{sw}^{min} = 70\,kHz$, and $F_{sw}^{max} = 170\,kHz$.

The parameters $N^{(U)}$ and $N^{(N)}$ in Eq. (9) are Utopia and Nadir points for the transformer turn ratio N. Suggested values for these two parameters may be $N^{(N)} = M_{dc}^{min}$ and $N^{(U)} = M_{dc}^{max}$. This is because the turn ratio parameter N directly impacts the voltage gain of the LLC converter (Eq. (1)), and the objective here is to minimize the parameter N for better efficiency, as mentioned earlier. The coefficients w_1, w_2, and w_3 in Eq. (9) are the weighted factors for the required minimum and maximum voltage gains and the transformer turn ratio, respectively. Keeping $w_1 + w_2 + w_3 = 1$ and changing the relationship between w_1, w_2, and w_3, a final converter design optimized for a minimum objective function $J(L_r, C_r, L_m, N)$ can be achieved. As can be seen in Eq. (9), the optimization algorithm diagrammed in Fig. 15 will endeavor to maintain the necessary voltage gain at the extremes of the frequency range required by the general converter specifications. Concurrently, the transformer turn ratio parameter N is kept as low as possible. It should be mentioned that the voltage gains $M_{dc}(\overline{x}, F_{sw}^{min})$ and $M_{dc}(\overline{x}, F_{sw}^{max})$ in Eq. (9) are calculated using the algorithm diagrammed in Fig. 6 for the LLC converter operating in constant power mode.

Fig. 15 presents an optimization algorithm for four parameters in the component's parameter space: L_r, C_r, L_m, and N. Multi-objective optimization is performed using the multivariable function minimization, which is based on a simple search method that uses unit vectors as a set of search directions or as a method of single-parameter variation [62, p. 413], [63, Section 3.2]. The next steps are as follows: First, parameter L_r alone is scanned to determine the local minimum of the objective function $J(L_r)$, and L_r—at which $J(L_r)$ is a local minimum—is kept fixed at the determined value until the next iteration of this step. Second, the parameter C_r is scanned to determine the local minimum

TABLE 2. Parameters for multi-object optimization for different cases.

	Case 1	Case 2	Case 3	Case 4
Opt. $L_r(H)$	1.15e-06	1.15e-06	3.44e-07	1.64e-06
Opt. $C_r(F)$	1.34e-06	2.55e-06	1.50e-06	1.05e-06
Opt. $L_m(H)$	1.55e-06	1.05e-05	7.77e-06	1.05e-05
Opt. N	4.15	4.17	3.333333	4.16
$L_r^{min}(H)$	1.0e-07	1.0e-07	1.0e-07	1.0e-07
$L_r^{max}(H)$	5.0e-06	5.0e-06	5.0e-06	5.0e-06
$C_r^{min}(F)$	1.0e-07	1.0e-07	1.0e-07	1.0e-07
$C_r^{max}(F)$	5.0e-06	5.0e-06	5.0e-06	2.0e-06
$L_m^{min}(H)$	1.0e-06	1.0e-06	1.0e-06	1.0e-06
$L_m^{max}(H)$	2.0e-05	2.0e-05	2.0e-05	2.0e-05
N^{min}	3.33	3.33	3.33	3.33
N^{max}	5.0	5.0	5.0	5.0
$w_1/w_2/w_3$	0.5/0.3/0.2	0.4/0.4/0.2	0.1/0.1/0.8	0.4/0.4/0.2

of the objective function. These same steps are performed for parameters L_m and N. The steps are repeated, cycling through the entire set of parameters $\bar{x} = \{L_r, C_r, L_m, N\}$ as many times as necessary, until the objective function stops decreasing. At the end of this series of four minimizations, the value of the objective function $J(L_r)$ is stored and compared against the previous value. If the current and previous values of the objective function are numerically close, with a relative accuracy ε, the process terminates with a list $\bar{x} = \{L_r, C_r, L_m, N\}$ of variables that can now be considered an optimized set of parameters, ready for verification via implementation in a design.

The result of the algorithm diagrammed in Fig. 15 will comprise a set of parameters $\bar{x}_{final} = \{L_r, C_r, L_m, N\}$ that can be used to design the fuel cell LLC converter practically. At this point, the design must be checked for ZVS in all frequency ranges and to confirm that the voltage gain characteristics do not have breaks similar to those in Figs. 8–10. If these issues are found, the weighted factor coefficients w_1, w_2, and w_3 may be changed and the optimization process can be repeated until a satisfactory result is obtained. As can also be seen in Figs. 8–10, the voltage gain characteristics exhibit a rapid reduction in the gain in the high frequency range; thus, the parameter F_{sw}^{max} can also be varied along with the weighted factor coefficients w_1, w_2, and w_3 for the final optimization of the converter using the algorithm diagrammed in Fig. 15. The parameters $\bar{x}_{final} = \{L_r, C_r, L_m, N\}$ are varied and scanned in the following corresponding limits: $L_r^{min} \ldots L_r^{max}$, $C_r^{min} \ldots C_r^{max}$, $L_m^{min} \ldots L_m^{max}$ and $N^{min} \ldots N^{max}$. Therefore, these limits can also be varied to obtain correct results; otherwise, for example, although the gain characteristic can be optimized, it can also be distorted if the resonant frequency $F_{rm} = \frac{1}{2\pi}\frac{1}{\sqrt{(L_r+L_m)C_r}}$ appears to fall between F_{sw}^{min} and F_{sw}^{max}.

The results of the implementation of the algorithms are presented in Fig. 16, showing the effect of different parameters on the final gain characteristics. The input parameters for the optimization in each case are presented in Table 2. Notably, Case 3 in Figs. 15 demonstrates that, theoretically, the minimum transformer turn ratio can be implemented as equal to the minimum required gain: $N^{opt} \approx M_{dc}^{min}$. However, in this instance, the voltage gain curve varies in the wide range when the frequency changes only slightly, and it has a steep form in the low-frequency range. Consequently, it is possible to predict that such a steep feature may present issues due to component tolerance, especially in multichannel setups with parallel connections on the primary and secondary sides. In this particular case, current balancing becomes an issue in the LF region. Due to the same mechanism, there may be channel output voltage differences if the secondary sides are connected in series. Another concern is the possible loss of ZVS in the low-frequency range.

Case 1, which is presented in Fig. 16, demonstrates the aforementioned situation in which the resonant frequency $F_{rm} = \frac{1}{2\pi}\frac{1}{\sqrt{(L_r+L_m)C_r}}$ appeared to fall between F_{sw}^{min} and F_{sw}^{max} due to a high initial specified C_r^{max}.

C. DESIGN PROCEDURE

The following are practical steps that can be performed to design an LLC converter with phase shift for fuel cell application:

- Design optimization using the algorithm diagrammed in Fig. 15 should be performed at the lowest possible minimum stack voltage V_{in}^{min} and the highest possible maximum stack current I_{in}^{max}. Thus, a constant power $P_{out} = V_{in}^{min} \cdot I_{in}^{max}$ is used as the converter power in the optimization algorithm.
- The weighted factors $w_1 = 0.4$, $w_2 = 0.4$ and $w_3 = 0.2$ can be used as a starting point.
- The voltage gain characteristics must be checked to confirm that there are no breaks, and they should be monotonous.
- Weighted factors and minimum and maximum frequencies may be varied as inputs to the optimization algorithm to achieve satisfactory voltage gain characteristics.
- After the converter parameters are returned by the algorithm, the converter should be checked for ZVS in the desired modes of operation.
- The designed converter should be analyzed for its components tolerance and distribution using, for example, the Monte-Carlo simulation.

Because the main application of the converter is a fuel cell system, the converter is optimized specifically for fuel cell characteristics. The fuel cell stack has a specific polarization curve, in which maximum power is reached at the lowest stack voltage (Fig. 1). Therefore, the minimum stack voltage and the maximum delivered power are the most critical parameters because the maximum current is delivered. This requires an accurate design methodology to achieve high efficiency, which is always challenging for low-voltage and high-current DC/DC converters. Furthermore, at this

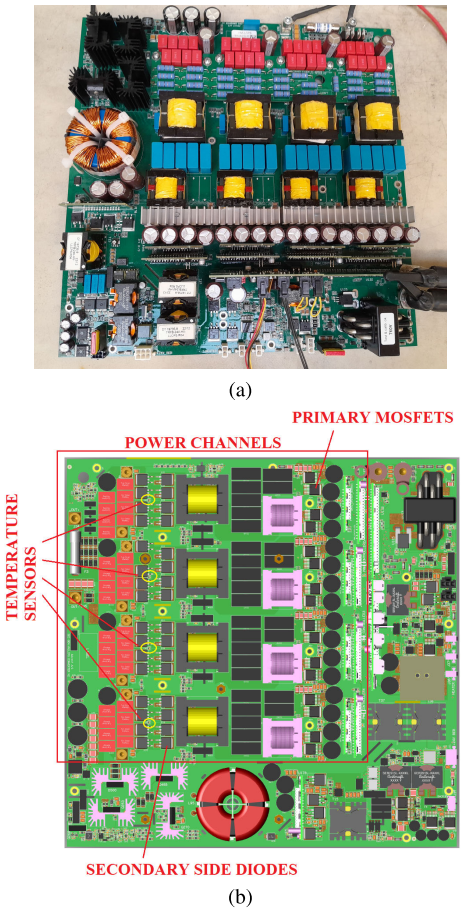

FIGURE 17. Prototype of the proposed LLC resonant converter for fuel cell application.

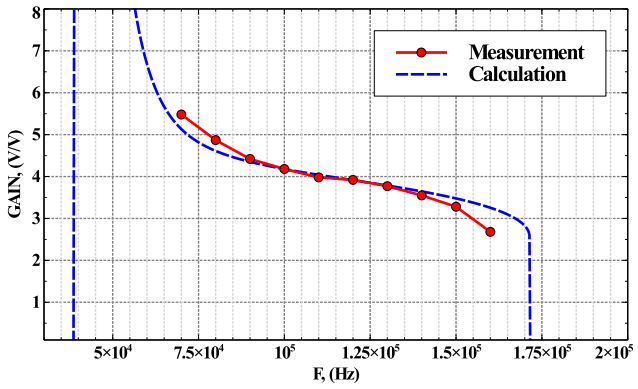

FIGURE 18. Comparison of the voltage gain obtained via calculation (algorithm diagrammed in Fig. 6) and the measured values. The converter operates in constant power mode, with parameters for the entire converter, and all channels are connected in parallel on the primary and secondary sides: $V_{in} = 60.0\,V$, and $I_{in} = 85\,A$.

voltage range, the converter should provide maximum voltage gain—especially at the highest load voltage. As mentioned earlier, maximum voltage gain at minimum stack voltage and maximum load voltage is one of the objectives of multi-objective optimization. To guarantee operation in another case (i.e., minimum stack voltage and minimum load voltage), the minimum voltage gain is also an element of optimization. It is important to have this case as an objective because it is still desirable to operate without phase shift under this condition to achieve high efficiency (fewer peak currents). The last optimized parameter is the turn ratio, N, which directly impacts efficiency, as mentioned earlier. Thus, the input parameters for the design procedure are as follows:

- Minimum stack voltage
- Maximum output power or maximum stack current
- Minimum and maximum battery (output) voltages
- Minimum and maximum switching frequencies

Notably, the maximum stack voltage is unnecessary in our design methodology because the required low-voltage gain is not a challenge for an LLC converter with phase shift. The phase shift between the legs of the LLC converter compensates for the excess gain at high input voltages, reducing the equivalent duty cycle.

Practical implementation of the algorithms diagrammed in Figs. 15 and 6 are written in the C programming language. The source code is available online [64] and as active media content in this paper.

VII. EXPERIMENT

A. VOLTAGE GAIN

To prove the concept of the LLC resonant converter working in constant power mode, a power converter board was designed and constructed, as illustrated in Fig. 17. The parameters of the constructed converter correspond to the parameters in Table 1. It should be noted that the parameters of the converter design were selected to be close to those in Case 4 in Table 2 in line with the reasoning discussed in Section VI.

A comparison of the voltage gain calculated using the algorithm diagrammed in Fig. 6 and the measured values achieved by the constructed converter is presented in Fig. 18. Here, the converter operates with a fixed stack voltage of 60 V and a constant current of 85 A; therefore, the converter transfers constant power to a load. Fig. 18 shows that the algorithm yields a good prediction of the gain characteristics; however, there are slight discrepancies at the minimum and maximum frequency regions, which can be explained by using FHA as the base for the LLC resonant converter modeling. It is evident that the measured gain at low frequencies is slightly higher than the calculated projections, which ensures that— with some margin—the necessary maximum gain can be reached at the minimum switching frequency. There is a similar situation with the high-frequency range, where the measured gain is slightly lower than the calculated projections. This ensures that the minimum gain can be achieved and the phase shift in the full-bridge converter stage will be close to 180°.

A critical observation in Fig. 18 must be emphasized. At especially high frequencies greater than the series resonance frequency $F_{rr} = \frac{1}{2\pi}\frac{1}{\sqrt{L_r C_r}}$, the calculated gain

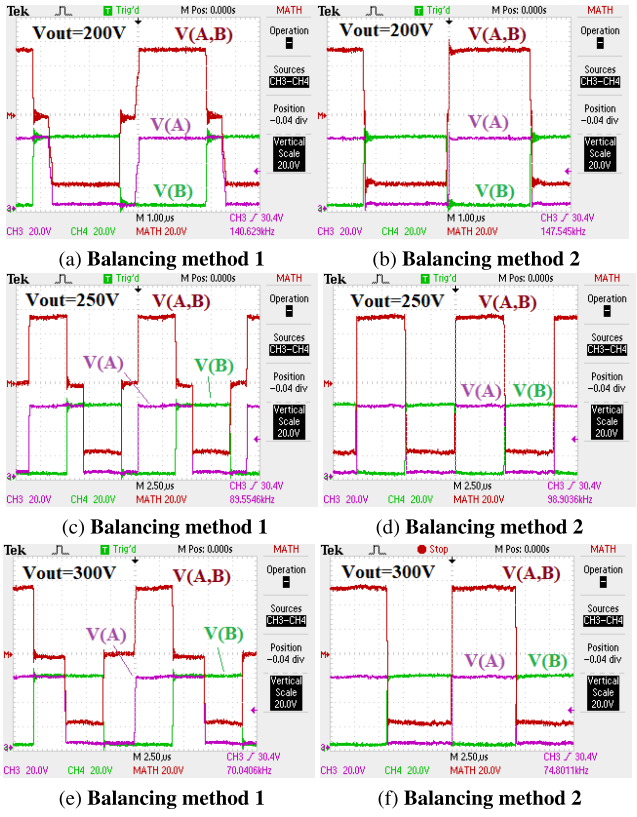

FIGURE 19. Primary side waveforms were measured for one of the channels of the converter, with two different approaches for channel current balancing. All left-side waveforms (a), (c), & (e) – Channel balancing using temperature measurement (method 1) and feed-forward switching frequency control; feed-forward control of the switching frequency is implemented using the algorithm diagrammed in Fig. 4, with parameter $K = 0.9$ (Section V-A). All right-side waveforms (b), (d), & (f): Channel balancing using adaptive switching frequency control (Section V-B, method 2). Total input current $I_{in} = 85\,A$, and stack voltage $V_{in} = 60\,V$. (a)–(b) $V_{out} = 200\,V$, (c)–(d) $V_{out} = 250\,V$, (e)–(f) $V_{out} = 300\,V$. CH3 is the drain-source of M2 (node A), CH4 is the drain-source of M4 (node B), and MATH is the difference between the CH3 and CH4 voltages on the full bridge [V(A, B)]. Regarding the switches, refer to Fig. 3.

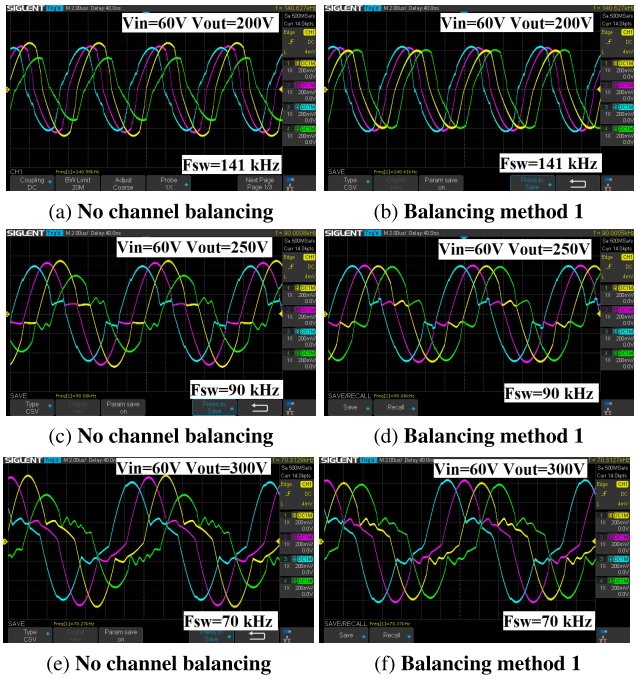

FIGURE 20. Measured values of the primary winding current in the main transformer T1 for all four channels, with and without channel balancing. Channel balancing is performed using the temperature measurements of each channel, as described in Section V-A (method 1). Feed-forward control of the switching frequency was implemented using the algorithm diagrammed in Fig. 4, with parameter $K = 0.9$. Current probe transfer coefficient: $90.9\,A/V$. (a), (c), & (e) – No channel balancing. (b), (d), & (f) – With channel balancing (method 1). (a) & (b) – $V_{out} = 200\,V$. (c) & (d) – $V_{out} = 250\,V$. (e) & (f) – $V_{out} = 300\,V$, $V_{in} = 60\,V$, and $I_{in} = 85\,A$.

is higher than the corresponding measured value. This means that when a feed-forward calculation of the switching frequency (Fig. 4, Section III) is employed, the real gain will be lower than projected. Therefore, in reality, a lower switching frequency is necessary to maintain a high enough voltage gain. One way to correct the switching frequency is to implement different coefficients K (Eq. (4)) for frequencies below F_{rr} and above F_{rr}. For example, $K = 1.0$ for the LF region, and $K = 0.9$ for the HF region.

B. PRIMARY SIDE WAVEFORMS

Fig. 19 presents the waveforms of the voltage in the legs of the full-bridge converter's primary side switches. Waveforms are taken as voltages at nodes A and B from Fig. 3. This figure also shows the phase shift difference with different channel balancing techniques, voltage difference between nodes A and B is also measured. All left-side waveforms represent the first technique of channel balancing, using the channel temperature measurement technique described in Section V-A, method 1. All right-side waveforms represent the second method, which is based on the self-balancing mechanism described in Section V-B, method 2. As expected, the self-balancing technique results in a phase shift between legs that is very close to 180° because the algorithm diagrammed in Fig. 14 tries to keep the frequency as high as possible to keep the stack current I_{in}^{meas} equal to the required current I_{in}^{set}.

C. CHANNEL BALANCING USING TEMPERATURE MEASUREMENTS

Fig. 20 show current balancing in all channels of the converter. Channel balancing was performed using the temperature measurements of each channel, as described in Section V-A, and feed-forward control of the switching frequency was implemented using the algorithm diagrammed in Fig. 4, with parameter $K = 0.9$. The current probe transfer coefficient was $90.9\,A/V$,; total input current $I_{in} = 85\,A$, and stack voltage $V_{in} = 60\,V$.

D. CHANNEL BALANCING USING THE SELF-BALANCING MECHANISM

Figs. 21 and 22 show the current balancing in all channels of the converter, but with the channel balancing performed using

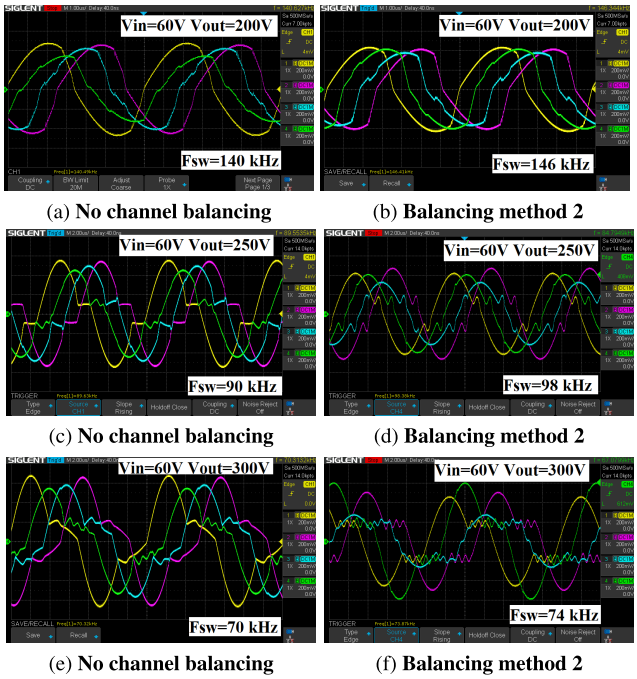

(a) No channel balancing (b) Balancing method 2
(c) No channel balancing (d) Balancing method 2
(e) No channel balancing (f) Balancing method 2

FIGURE 21. Measured values of the primary winding current in the main transformer T1 for all four channels, with and without channel balancing. Channel balancing performed using the self-balancing mechanism described in Section V-B (method 2). $V_{in} = 60\,V$. $I_{in} = 85\,A$. (a), (c), & (e): no channel balancing; (b), (d), & (f): with channel balancing (method 2); (a) & (b): $V_{out} = 200\,V$; (c) & (d): $V_{out} = 250\,V$; (e) & (f): $V_{out} = 300\,V$. The screenshot in (d) presents the instability waveform for the $V_{out} = 250\,V$ case, and the instability waveforms in (f) are for the $V_{out} = 300\,V$ case.

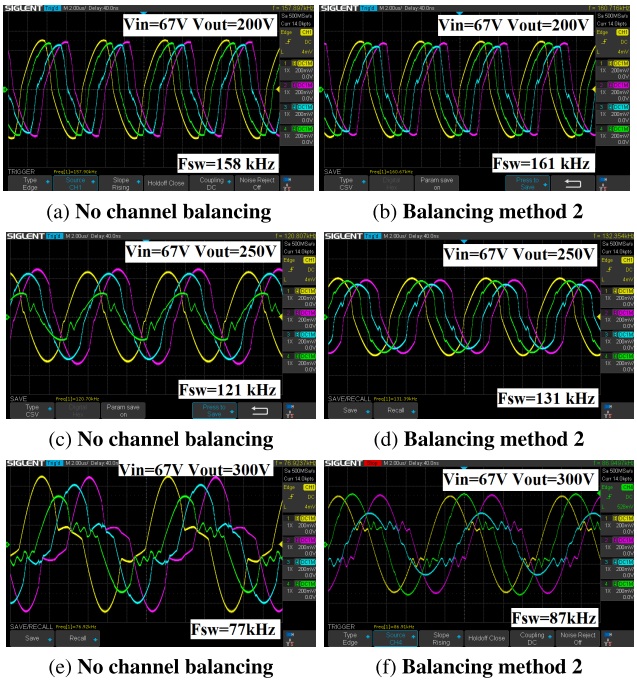

(a) No channel balancing (b) Balancing method 2
(c) No channel balancing (d) Balancing method 2
(e) No channel balancing (f) Balancing method 2

FIGURE 22. Measured values of the primary winding current in the main transformer T1 for all four channels, with and without channel balancing. Channel balancing is performed using the self-balancing mechanism described in Section V-B (method 2). $V_{in} = 67\,V$ and $I_{in} = 85\,A$. (a), (c), & (e): no channel balancing; (b), (d), & (f): with channel balancing (method 2); (a) & (b): $V_{out} = 200\,V$; (c) & (d): $V_{out} = 250\,V$; (e) & (f) – $V_{out} = 300\,V$. The screenshot in (f) presents the instability waveform for the $V_{out} = 300\,V$ case.

the self-balancing mechanism described in Section V-B. As expected, some instability is noticeable at the low-frequency range, as discussed in Section V-B. This instability was captured, and it can be seen in Figs. 21d and 21f for the 60 V stack voltage and the 250 V and 300 V load voltages. For the 67 V of stack voltage, the instability was captured only for the 300 V load voltage, and can be seen in Fig. 22f. The superior stability of the higher stack voltage is attributable to the fact that the required voltage gain in this case is less than for the lower stack current. Thus, the converter operates in a higher switching frequency range in which the self-balancing mechanism is successful, as described in Section V-B.

E. EFFICIENCY MEASUREMENT

Figs. 23 - 26 present an efficiency comparison for the cases in which channel balancing was disabled and then enabled for only two stack voltages: 60 V and 67 V. The channel balancing effect on efficiency is demonstrated using only the temperature measurements of each channel, as described in Section V-A (method 1), as it proved to be the most stable approach. The figures prove that channel balancing is definitely necessary for improved efficiency and a significantly long life span for the converter.

Switching frequency ranges and their effect on efficiency are also demonstrated for the same conditions (Figs. 24 and 26). Notably, the highest efficiency is reached at the same switching frequency despite differences in the input stack voltage. This effect can be further investigated in future research. The optimized region of operation can be determined by taking the two graphs above (efficiency vs. output voltage, and efficiency vs. switching frequency) into consideration. The data on all the efficiency measurements illustrated in Figs. 23 - 26 are presented in Tables 3 and 4.

TABLE 3. Efficiency measurements results. $V_{in} = 60\,V$. $I_{in} = 85\,A$.

V_{out}, (V)	Eff., %, no balancing	Eff., %, with balancing (method 1)	F_{sw}, (kHz)
200	95.0	95.5	141
225	95.5	96.2	119
250	95.2	95.6	90
275	94.1	94.6	72
300	93.8	94.8	70

F. EMI CONSIDERATIONS

The proposed converter was part of the fuel cell system tested for electromagnetic interference (EMI) and EMC. The most challenging tests to pass were conducted, and the radiated emissions were measured.

A summary of the EMI improvement techniques applicable to the proposed LLC converter is presented below.

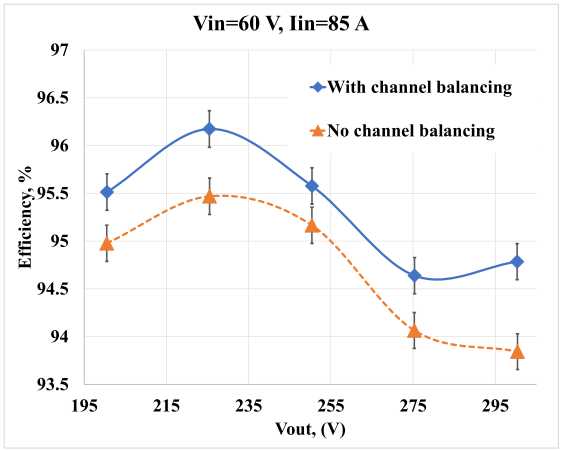

FIGURE 23. Efficiency vs. output voltage of the converter with and without channel current balancing. Channel balancing is performed using the temperature measurements of each channel, as described in Section V-A (method 1). Feed-forward control of the switching frequency is implemented using the algorithm diagrammed in Fig. 4, with parameter $K = 0.9$. Total input current $I_{in} = 85\,A$, and stack voltage $V_{in} = 60\,V$.

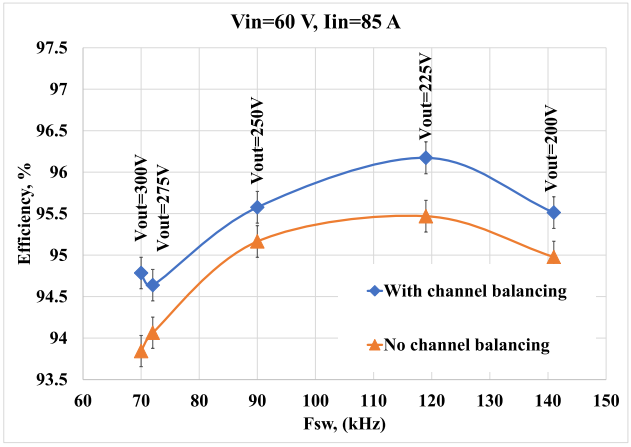

FIGURE 24. Efficiency vs. switching frequency of the converter with and without channel current balancing. Channel balancing is performed using the temperature measurements of each channel, as described in Section V-A (method 1). Feed-forward control of the switching frequency is implemented using the algorithm diagrammed in Fig. 4, with parameter $K = 0.9$. Total input current $I_{in} = 85\,A$, and stack voltage $V_{in} = 60\,V$.

TABLE 4. Efficiency measurements results. $V_{in} = 67\,V$. $I_{in} = 85\,A$.

V_{out}, (V)	Eff., %, no balancing	Eff., %, with balancing (method 1)	F_{sw}, (kHz)
200	94.6	94.8	158
225	95.5	95.7	144
250	95.8	96.3	121
275	95.5	95.9	94
300	94.5	95.0	77

- MCU software-defined spread spectrum for switching frequency harmonics.
- ZVS for primary switches.

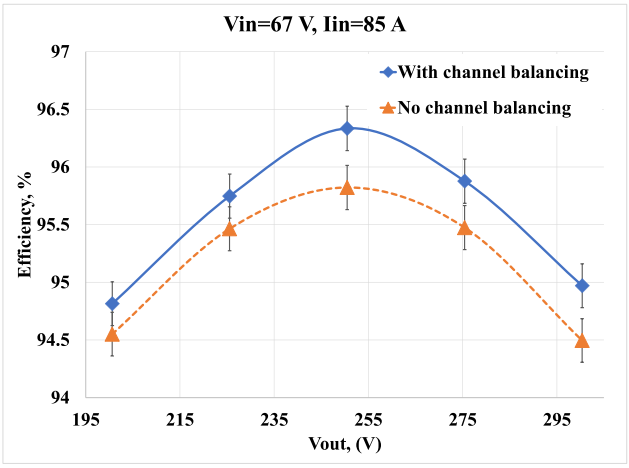

FIGURE 25. Efficiency vs. output voltage of the converter with and without channel current balancing. Channel balancing is performed using the temperature measurements of each channel, as described in Section V-A (method 1). Feed-forward control of the switching frequency is implemented using the algorithm diagrammed in Fig. 4, with parameter $K = 0.9$. Total input current $I_{in} = 85\,A$, and stack voltage $V_{in} = 60\,V$.

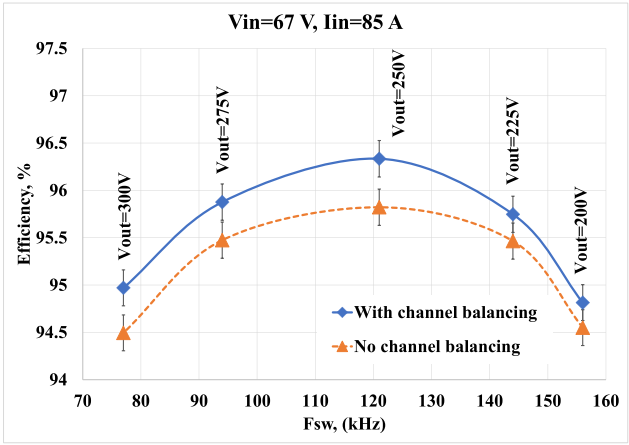

FIGURE 26. Efficiency vs. switching frequency of the converter with and without channel current balancing. Channel balancing is performed using the temperature measurements of each channel, as described in Section V-A (method 1). Feed-forward control of the switching frequency is implemented using the algorithm diagrammed in Fig. 4, with parameter $K = 0.9$. Total input current $I_{in} = 85\,A$, and stack voltage $V_{in} = 60\,V$.

- Control of dv/dt rate by placing additional capacitance in parallel with each MOSFET.
- Snubber circuits across MOSFETs and output diodes.
- di/dt controlled by gate drive turn-on/off resistance.
- Cable radiation is improved by implementing ferrite beads on internal cables
- Internal cables are also optimized and placed as far as possible from switching parts (inductors, transformers, MOSFETs).

VIII. CONCLUSION

This study presents a multichannel phase shift LLC resonant converter with a wide input and output voltage range that has been customized for fuel cell applications. The battery

TABLE 5. Comparison of methods of LLC resonant converter optimization.

Ref.	Calculation method	Optimization method	Objective function's components	Design variables	$\mathbf{V_{in}}$, $\mathbf{V_{out}}$, $\mathbf{F_{sw}}$ ranges (for design and optimization)	$\mathbf{R_L/P_{out}}$ mode
[27]	Time domain mode solver	MATLAB optimization search engine is applied	• Total loss • V_{out}	F_{sw}, N, L_m, C_r, L_r, transformer design	$F_{sw} \approx F_r$ $V_{in} = 400\,V$ $V_{out} = 12\,V$	Constant R_L
[28] [29]	Time domain mode solver	Peak gain placement design procedure, MATLAB engine is applied	• Power losses • Peak gain	L_r, C_r, L_m, N	$F_{sw} = 80 - 160\,kHz$ $F_r = 140\,kHz$ $V_{in} = 25 - 38\,V$ $V_{out} = 400\,V$	Constant R_L
[49]	Time domain analysis	Method based on unified time domain operation stage trajectories	• RMS current in inductors L_r and L_m • Peak resonance current • Peak resonance voltage across C_r	Duty cycle and F_{sw}	$F_{sw} = 75 - 150\,kHz$ $V_{in} = 300\,V$ $V_{out} = 300\,V$	Constant R_L
[50]	Time domain numerical analysis	Surrogate model based on adaptive polynomial approximation method	• Primary RMS current • Secondary RMS current • Losses in core of the transformer	L_r, C_r, L_m	$F_{sw} < F_r$ $V_{in} = 260 - 360\,V$ $V_{out} = 48\,V$	Constant R_L
[51]	Time domain mode solver	MATLAB optimization search engine is applied (the fmincon routine)	• The cost function of this optimization is to minimize the losses at full load, which is denoted by $P_{loss} = P_{pri} + P_{sec} + P_{trafo}$	L_r, C_r, L_m, N	$F_{sw} \approx F_r = 115\,kHz$ $V_{in} = 30\,V$ $V_{out} = 403\,V$	Constant R_L
[52]	Frequency domain impedance model	Swarm Parameter Optimization	• Loss Breakdown • Voltage Gain	L_r, C_r, L_m, L_{aux}, R_{aux}	$F_{sw} \approx F_r$ $V_{in} = 60\,V$ $V_{out} = 60\,V$	Constant R_L
[53]	Time domain mode solver	Variable-step exhaustive search algorithm	• Time-Weighted Average Efficiency (during battery charging), 4 points • M_{max} and M_{min} • Peak resonance voltage across C_r	L_r, C_r, L_m	$F_{sw} = 120 - 250\,kHz$ $V_{in} = 400\,V$ $V_{out} = 60 - 100\,V$	Constant R_L for each state-of-charge point
[54]	Time domain analysis	Newton or Quasi-Newton algorithm, MATLAB optimization search engine	• Limiting the starting current in the load by optimizing the selection of the C_{out} filter capacitor and • simultaneously preventing large voltage pulsations in the established mode	C_{out}	$F_{sw} = 80 - 150\,kHz$ $V_{in} = 375 - 405\,V$ $V_{out} = 12\,V$	Constant R_L

TABLE 5. *(Continued.)* **Comparison of methods of LLC resonant converter optimization.**

[55]	Steady State Analysis (time domain)	Flow chart of LLC parameters optimization procedure	• Goal is to reach M_{max} at lowest frequency	L_m	$F_{sw} = 120 - 180\,kHz$ $V_{in} = 400\,V$ $V_{out} = 50 - 100\,V$	Constant R_L, determined at nominal conditions
[56]	FHA	Genetic algorithm is executed using MATLAB software	• The fitness function is defined as: $min\frac{-dM_{dc}(F_{sw},L_r,C_r,L_m,N)}{dF_{sw}}$ • Constrain Functions: $M_{min} < M_{dc} < M_{max}$, ZVS	L_r, C_r, L_m, N	$F_{sw} = 100 - 120\,kHz$ $V_{in} = 200 - 400\,V$ $V_{out} = 48\,V$, no experiment	Constant R_L
[57]	Time domain analysis	Exhaustive search method, particle swarm optimization (PSO), genetic algorithm (GA), An automated optimal design tool using MATLAB	• Inductor RMS current • Resonant capacitor voltage stress • Maximum voltage gain requirement	L_r, C_r, L_m	$F_{sw} = 60 - 150\,kHz$ $V_{in} = 250 - 420\,V$ $V_{out} = 400\,V$	Constant R_L
[58]		Designed algorithm	• Start-up current requirement • Maximum DC gain requirement • Optimum efficiency at nominal voltage	L_r, C_r, L_m	$F_{sw} = 720 - 1000\,kHz$ $V_{in} = 370 - 410\,V$ $V_{out} = 12\,V$	Constant R_L
[59] [60]	Time domain analysis	Firefly Algorithm	• Output voltage • Peak value of resonant current	• L_r, C_r • Time constant of the exponential frequency sweep	$F_{sw} = 600\,kHz$ $V_{in} = 390\,V$ $V_{out} = 24\,V$	Constant P_{out}
[61]	Time domain analysis and FHA	Search algorithm	• Weighted Average Efficiency (during battery charging), 4 points • System volume • System cost	L_r, C_r, L_m, Switches, Magnetics	$F_{sw} = 120 - 250\,kHz$ $V_{in} = 370 - 430\,V$ $V_{out} = 48 - 54\,V$	Constant R_L for each state-of-charge point
This work	FHA	Simple search method that used unit vectors as a set of search directions, Method of single parameter variation	• M_{max} and M_{min} • lowest possible N	L_r, C_r, L_m, and N	$F_{sw} = 70 - 250\,kHz$ $V_{in} = 60 - 120\,V$ $V_{out} = 200 - 300\,V$	Constant P_{out}

voltage range and the worst-case polarization curve of the fuel cell are utilized to determine the optimum parameters for an LLC converter. The algorithm for such a computation is presented, taking into account the voltage gain of the converter running at constant power. Instead of expending resources on expensive current measurements, channel temperature readings are used to perform current balancing. For converters running at high frequencies—greater than the series resonance frequency of a resonant converter—a natural self-balancing mechanism was investigated. Suggestions for maximizing efficiency via the transformer turn ratio of the converter are provided.

Multi-object optimization is applied to achieve an optimal design, which allows for achieving the minimum and maximum voltage gains while maintaining a low transformer turn ratio for high efficiency. Thus, the optimal design of the LLC converter is guaranteed by the following rationale:

- First, we define our design goals: The converter for the fuel cell must operate across a wide range of both input and output voltages. The system requires an input voltage range V_{in}=60-120V and an output voltage range V_{out}=200-300V. At the same time, the converter must have relatively high efficiency; hence, it must employ a one-stage energy conversion. As described earlier, an LLC converter with phase shift has been selected. In this study, it has been explained that such a converter will have a particularly high efficiency if it has a transformer with the minimum possible turn ratio, N, where $N = N_{sec}/N_{pri}$. In this case, the secondary RMS current—which depends primarily on the load power—will be reflected to the primary side at the minimum possible primary RMS current. This low current guarantees low conducted and switching losses and, thus, an increase in overall efficiency. Therefore, the objective function is formulated in line with the following rationale: For high efficiency, we need to achieve minimum and maximum gains along with a minimum turn ratio value N. Alternative optimization methods are presented in Table 5.
- We then developed an algorithm that produced an optimized design, with the parameters L_r, C_r, L_m, and N as the output. Our algorithm is included as a media file, is realized in C-language, and can easily be utilized using any C-compiler. Different design variants are possible; these may be employed to obtain varying weighted factors for the objective function.
- The parameters L_r, C_r, L_m, and N fully determine the LLC converter design and can be used for further calculation of the converter and time-domain simulation. Design variants can be compared for the best match of gain characteristics with stability such that there are no breaks in the optimized characteristic.
- Finally, an experimental prototype is tested to evaluate the waveforms, gain characteristics, and efficiency.

A four-channel converter experimental prototype is implemented and tested at a 5 kW power level. Active content and the C language code files for converter calculations are also supplied in this paper.

APPENDIX

See Table 5.

ACKNOWLEDGMENT

The authors would like to thank SøRen Juhl Andreasen and Christian Rostgaard Andersen from Advent Technologies A/S for the support and assistance with this research.

REFERENCES

[1] K. K. Justesen, "Reformed methanol fuel cell systems-and their use in electric hybrid systems," Doctoral dissertation, Dept. Energy Technol., Aalborg Univ., Copenhagen, Denmark, 2015.
[2] *Nordbjærgs Bådeværft A/S, Fremtidens Båd*. Accessed: May 11, 2024. [Online]. Available: https://nordbjaergs.dk/baadevaerft/
[3] *Nordbjrgs Bdevrft A/S*. Accessed: May 11, 2024. [Online]. Available: https://nordbjaergs.dk/baadevaerft/
[4] *Case Story: Motorola Norway*. Accessed: May 11, 2024. [Online]. Available: https://serene.advent.energy/motorola/
[5] *Telefnica Germany*. Accessed: May 11, 2024. [Online]. Available: https://youtu.be/aVL8L5M-Klc?si=9wb1nHIYxTMMiklV
[6] *HiPower Green Tech*. Accessed: May 11, 2024. [Online]. Available: https://www.hipower.ltd/post/mini-mgen-rolling-out
[7] A. Andreiciks, I. Steiks, and O. Krievs, "Design of efficient current fed DC/DC converter for fuel cell applications," in *Proc. IEEE Int. Symp. Ind. Electron.*, Jun. 2011, pp. 206–210, doi: 10.1109/ISIE.2011.5984158.
[8] L. P. Petersen, L. C. Jensen, and M. N. Larsen, "High efficiency isolated DC/DC converter inherently optimized for fuel cell applications," in *Proc. 15th Eur. Conf. Power Electron. Appl. (EPE)*, Sep. 2013, pp. 1–10, doi: 10.1109/EPE.2013.6634709.
[9] M. Rosekeit, J. Burkard, M. Lelie, D. U. Sauer, and R. W. De Doncker, "Full-bridge DC–DC converter with planar transformer and center-tap rectifier for fuel cell powered uninterruptible power supply," in *Proc. 16th Eur. Conf. Power Electron. Appl.*, Aug. 2014, pp. 1–10, doi: 10.1109/EPE.2014.6910884.
[10] B. M. Han, J.-Y. Lee, and Y.-S. Jeong, "Power conditioning system for fuel cell with 2-stage DC–DC converter," in *Proc. 25th Annu. IEEE Appl. Power Electron. Conf. Expo. (APEC)*, Feb. 2010, pp. 303–308, doi: 10.1109/APEC.2010.5433656.
[11] H. Huang, "Designing an LLC resonant half-bridge power converter," in *Texas Instruments Power Supply Design Seminar*, vol. 3. Dallas, TX, USA: Texas Instruments Incorporated Dallas, 2010. Accessed: May 11, 2024. [Online]. Available: https://bbs.dianyuan.com/upload/community/2013/12/01/1385867010-65563.pdf
[12] J. Lu and A. Khaligh, "1kW, 400 V/12 V high step-down DC/DC converter: Comparison between phase-shifted full-bridge and LLC resonant converters," in *Proc. IEEE Transp. Electrific. Conf. Expo (ITEC)*, Jun. 2017, pp. 275–280.
[13] C. Zhao, X. Wu, and Z. Qian, "Design and comparison of two front-end DC/DC converters: LLC resonant converter and soft-switched phase-shifted full-bridge converter with primary-side energy storage inductor," in *Proc. 24th Annu. IEEE Appl. Power Electron. Conf. Expo.*, Feb. 2009, pp. 1073–1077, doi: 10.1109/APEC.2009.4802796.
[14] H. Wang and Z. Li, "A PWM LLC type resonant converter adapted to wide output range in PEV charging applications," *IEEE Trans. Power Electron.*, vol. 33, no. 5, pp. 3791–3801, May 2018, doi: 10.1109/TPEL.2017.2713815.
[15] A. Amirahmadi, M. Domb, and E. Persson, "High power density high efficiency wide input voltage range LLC resonant converter utilizing E-mode GaN switches," in *Proc. IEEE Appl. Power Electron. Conf. Expo. (APEC)*, Mar. 2017, pp. 350–354, doi: 10.1109/APEC.2017.7930716.
[16] W. Ma, X. Xie, and S. Jiang, "LLC resonant converter with variable resonant inductor for wide LED dimming range," in *Proc. IEEE Appl. Power Electron. Conf. Expo. (APEC)*, Mar. 2017, pp. 2950–2957, doi: 10.1109/APEC.2017.7931116.
[17] H. Wu, X. Zhan, and Y. Xing, "Interleaved LLC resonant converter with hybrid rectifier and variable-frequency plus phase-shift control for wide output voltage range applications," *IEEE Trans. Power Electron.*, vol. 32, no. 6, pp. 4246–4257, Jun. 2017, doi: 10.1109/TPEL.2016.2602545.

[18] H. Lin, X. Jin, W. Yao, Z. Lyu, Y. Deng, and X. Sun, "A vary mode control-based high-efficiency full-bridge LLC resonant converter operating in super wide input voltage range," in *Proc. IEEE 2nd Annu. Southern Power Electron. Conf. (SPEC)*, Dec. 2016, pp. 1–5, doi: 10.1109/SPEC.2016.7846047.

[19] H.-G. Han, Y.-J. Choi, S.-Y. Choi, and R.-Y. Kim, "A high efficiency LLC resonant converter with wide ranged output voltage using adaptive turn ratio scheme for a Li-ion battery charger," in *Proc. IEEE Vehicle Power Propuls. Conf. (VPPC)*, Oct. 2016, pp. 1–6, doi: 10.1109/VPPC.2016.7791570.

[20] B. Lin and C. Chu, "Hybrid full-bridge and LLC converter with wide ZVS range and less output inductance," *IET Power Electron.*, vol. 9, no. 2, pp. 377–384, Feb. 2016, doi: 10.1049/iet-pel.2014.0991.

[21] X. Jin, H. Hu, H. Wu, and X. Ma, "A LLC resonant converter with a notch filter at secondary side for high step-up and wide voltage range applications," in *Proc. IEEE 2nd Int. Future Energy Electron. Conf. (IFEEC)*, Nov. 2015, pp. 1–5, doi: 10.1109/IFEEC.2015.7361402.

[22] M. M. Jovanovic and B. T. Irving, "Efficiency optimization of LLC resonant converters operating in wide input- and/or output-voltage range by on-the-fly topology-morphing control," in *Proc. IEEE Appl. Power Electron. Conf. Expo. (APEC)*, Mar. 2015, pp. 1420–1427, doi: 10.1109/APEC.2015.7104534.

[23] T. Mishima, H. Mizutani, and M. Nakaoka, "A sensitivity-improved PFM LC resonant full-bridge DC–DC converter with LC antiresonant circuitry," *IEEE Trans. Power Electron.*, vol. 32, no. 1, pp. 310–324, Jan. 2017, doi: 10.1109/TPEL.2016.2524640.

[24] S. M. S. I. Shakib and S. Mekhilef, "A frequency adaptive phase shift modulation control based LLC series resonant converter for wide input voltage applications," *IEEE Trans. Power Electron.*, vol. 32, no. 11, pp. 8360–8370, Nov. 2017, doi: 10.1109/TPEL.2016.2643006.

[25] M. Kim, S. Noh, and S. Choi, "New parallel loaded resonant converter with wide input and output voltage range," in *Proc. 9th Int. Conf. Power Electron. ECCE Asia (ICPE-ECCE Asia)*, Jun. 2015, pp. 515–520, doi: 10.1109/ICPE.2015.7167834.

[26] C.-E. Kim, J.-I. Baek, and J.-B. Lee, "High-efficiency single-stage LLC resonant converter for wide-input-voltage range," *IEEE Trans. Power Electron.*, vol. 33, no. 9, pp. 7832–7840, Sep. 2018, doi: 10.1109/TPEL.2017.2772443.

[27] R. Yu, G. K. Y. Ho, B. M. H. Pong, B. W. Ling, and J. Lam, "Computer-aided design and optimization of high-efficiency LLC series resonant converter," *IEEE Trans. Power Electron.*, vol. 27, no. 7, pp. 3243–3256, Jul. 2012, doi: 10.1109/TPEL.2011.2179562.

[28] X. Fang, H. Hu, F. Chen, U. Somani, E. Auadisian, J. Shen, and I. Batarseh, "Efficiency-oriented optimal design of the LLC resonant converter based on peak gain placement," *IEEE Trans. Power Electron.*, vol. 28, no. 5, pp. 2285–2296, May 2013, doi: 10.1109/TPEL.2012.2211895.

[29] X. Fang, H. Hu, J. Shen, and I. Batarseh, "An optimal design of the LLC resonant converter based on peak gain estimation," in *Proc. 27th Annu. IEEE Appl. Power Electron. Conf. Expo. (APEC)*, Orlando, FL, USA, Feb. 2012, pp. 1286–1291, doi: 10.1109/APEC.2012.6165984.

[30] J. Yamamoto, T. Zaitsu, S. Abe, and T. Ninomiya, "PFM and PWM hybrid controlled LLC converter," in *Proc. Int. Power Electron. Conf. (IPEC-Hiroshima-ECCE ASIA)*, May 2014, pp. 177–182, doi: 10.1109/ipec.2014.6869577.

[31] J.-H. Kim, C.-E. Kim, J.-K. Kim, J.-B. Lee, and G.-W. Moon, "Analysis on load-adaptive phase-shift control for high efficiency full-bridge LLC resonant converter under light-load conditions," *IEEE Trans. Power Electron.*, vol. 31, no. 7, pp. 4942–4955, Jul. 2016, doi: 10.1109/TPEL.2015.2462077.

[32] Y.-K. Lo, C.-Y. Lin, M.-T. Hsieh, and C.-Y. Lin, "Phase-shifted full-bridge series-resonant DC–DC converters for wide load variations," *IEEE Trans. Ind. Electron.*, vol. 58, no. 6, pp. 2572–2575, Jun. 2011, doi: 10.1109/TIE.2010.2058076.

[33] B. McDonald and F. Wang, "LLC performance enhancements with frequency and phase shift modulation control," in *Proc. IEEE Appl. Power Electron. Conf. Expo. (APEC)*, Mar. 2014, pp. 2036–2040, doi: 10.1109/APEC.2014.6803586.

[34] X. Wu, Z. Bai, and H. Ma, "An LLC converter operating in super-wide output voltage range with variable-mode control strategy," in *Proc. IEEE Int. Power Electron. Appl. Conf. Expo. (PEAC)*, Nov. 2018, pp. 1–6, doi: 10.1109/PEAC.2018.8590324.

[35] Y. Shen, H. Wang, F. Blaabjerg, X. Sun, and X. Li, "Analytical model for LLC resonant converter with variable duty-cycle control," in *Proc. IEEE Energy Convers. Congr. Expo. (ECCE)*, Sep. 2016, pp. 1–7, doi: 10.1109/ECCE.2016.7854882.

[36] H. Wang, Y. Chen, Y. Qiu, P. Fang, Y. Zhang, L. Wang, Y.-F. Liu, J. Afsharian, and Z. Yang, "Common capacitor multiphase LLC converter with passive current sharing ability," *IEEE Trans. Power Electron.*, vol. 33, no. 1, pp. 370–387, Jan. 2018, doi: 10.1109/TPEL.2017.2661066.

[37] Z. Hu, Y. Qiu, Y.-F. Liu, and P. C. Sen, "An interleaving and load sharing method for multiphase LLC converters," in *Proc. 37th Annu. IEEE Appl. Power Electron. Conf. Expo. (APEC)*, Mar. 2013, pp. 1421–1428, doi: 10.1109/APEC.2013.6520485.

[38] Z. Hu, Y. Qiu, and Y.-F. Liu, "Digital implementation of load sharing method for interleaved LLC converters," in *Proc. IEEE 14th Workshop Control Modeling Power Electron. (COMPEL)*, Jun. 2013, pp. 1–7, doi: 10.1109/COMPEL.2013.6626420.

[39] H. Chen, X. Wu, F. Peng, Z. Qian, and C. Hu, "Current balance method for the two-phase interleaved LLC-RDCX with parallel PWM output regulation," in *Proc. Int. Power Electron. Appl. Conf. Expo.*, Nov. 2014, pp. 136–141, doi: 10.1109/PEAC.2014.7037843.

[40] H. Wang, Y. Chen, and Y.-F. Liu, "A passive-impedance-matching technology to achieve automatic current sharing for a multiphase resonant converter," *IEEE Trans. Power Electron.*, vol. 32, no. 12, pp. 9191–9209, Dec. 2017, doi: 10.1109/TPEL.2017.2653081.

[41] H. Wang, Y. Chen, Y.-F. Liu, J. Afsharian, and Z. Yang, "A passive current sharing method with common inductor multiphase LLC resonant converter," *IEEE Trans. Power Electron.*, vol. 32, no. 9, pp. 6994–7010, Sep. 2017, doi: 10.1109/TPEL.2016.2626312.

[42] Y. Chen and Y.-F. Liu, "Latest advances of LLC converters in high current, fast dynamic response, and wide voltage range applications," *CPSS Trans. Power Electron. Appl.*, vol. 2, no. 1, pp. 59–67, 2017, doi: 10.24295/CPSSTPEA.2017.00007.

[43] M. Noah, J. Imaoka, Y. Ishikura, K. Umetani, and M. Yamamoto, "Review of current balance mechanism in multiphase LLC resonant converters," in *Proc. IEEE 27th Int. Symp. Ind. Electron. (ISIE)*, Jun. 2018, pp. 1030–1036, doi: 10.1109/ISIE.2018.8433827.

[44] O. Kirshenboim and M. M. Peretz, "Combined multilevel and two-phase interleaved LLC converter with enhanced power processing characteristics and natural current sharing," *IEEE Trans. Power Electron.*, vol. 33, no. 7, pp. 5613–5620, Jul. 2018, doi: 10.1109/TPEL.2017.2740342.

[45] H. Wang, Y. Chen, Y.-F. Liu, and P. C. Sen, "A general multi-phase coupled-resonant-tank resonant converter," in *Proc. IEEE Appl. Power Electron. Conf. Expo. (APEC)*, Mar. 2018, pp. 2183–2190, doi: 10.1109/APEC.2018.8341319.

[46] H. Wang, Y. Chen, Y.-F. Liu, Z. A. Yang, J. Afsharian, and B. Gong, "LLC resonant converter with shared power switches and dual coupled resonant tanks to achieve automatic current sharing," in *Proc. IEEE Energy Convers. Congr. Expo. (ECCE)*, Oct. 2017, pp. 5712–5719, doi: 10.1109/ECCE.2017.8096949.

[47] A. J. Hanson and D. J. Perreault, "Modeling the magnetic behavior of N-winding components: Approaches for unshackling switching superheroes," *IEEE Power Electron. Mag.*, vol. 7, no. 1, pp. 35–45, Mar. 2020, doi: 10.1109/MPEL.2019.2959356.

[48] M. H. Ahmed, M. A. de Rooij, and J. Wang, "High-power density, 900-W LLC converters for servers using GaN FETs: Toward greater efficiency and power density in 48 v to 612 v converters," *IEEE Power Electron. Mag.*, vol. 6, no. 1, pp. 40–47, Mar. 2019, doi: 10.1109/mpel.2018.2886106.

[49] Z. Xiao, Z. He, Y. Ning, H. Wang, A. Luo, Y. Chen, and J. Chen, "Optimization of LLC resonant converter with two degrees of freedom based on operation stage trajectory analysis," *IEEE Access*, vol. 9, pp. 79629–79642, 2021, doi: 10.1109/ACCESS.2021.3083100.

[50] B. Zhou, M. Zhang, H. Luo, Y. Qiu, S. Chen, T. Zang, Y. Zhou, and X. Zhou, "Multi-objectives optimization of parameter design for LLC converter based on data-driven surrogate model," *IET Power Electron.*, vol. 116, May 2023, doi: 10.1049/pel2.12525.

[51] U. Mumtahina and P. J. Wolfs, "Multimode optimization of the phase-shifted LLC series resonant converter," *IEEE Trans. Power Electron.*, vol. 33, no. 12, pp. 10478–10489, Dec. 2018, doi: 10.1109/TPEL.2018.2803741.

[52] X. Han, X. Yao, and Y. Liao, "Full operating range optimization design method of LLC resonant converter in marine DC power supply system," *J. Mar. Sci. Eng.*, vol. 11, no. 11, p. 2142, Nov. 2023, doi: 10.3390/jmse11112142.

[53] Z. Fang, T. Cai, S. Duan, and C. Chen, "Optimal design methodology for LLC resonant converter in battery charging applications based on time-weighted average efficiency," *IEEE Trans. Power Electron.*, vol. 30, no. 10, pp. 5469–5483, Oct. 2015, doi: 10.1109/TPEL.2014.2379278.

[54] N. Hinov, B. Gilev, and T. Hranov, "Model-based optimization of an LLC-resonant DC–DC converter," *Electronics*, vol. 8, no. 7, p. 799, Jul. 2019, doi: 10.3390/electronics8070799.
[55] Z. Fang, S. Duan, C. Chen, X. Chen, and J. Zhang, "Optimal design method for LLC resonant converter with wide range output voltage," in *Proc. 28th Annu. IEEE Appl. Power Electron. Conf. Expo. (APEC)*, Long Beach, CA, USA, Mar. 2013, pp. 2106–2111, doi: 10.1109/APEC.2013.6520586.
[56] E. Khoobroo, B. Ashrafinia, and M. Akhbari, "Optimal design of LLC resonant converter with improved controllability," in *Proc. 5th Annu. Int. Power Electron., Drive Syst. Technol. Conf. (PEDSTC)*, Tehran, Iran, Feb. 2014, pp. 396–401, doi: 10.1109/PEDSTC.2014.6799407.
[57] Y. Wei, T. Pereira, Y. Pan, M. Liserre, F. Blaabjerg, and H. A. Mantooth, "A general and automatic RMS current oriented optimal design tool for LLC resonant converters," *IEEE J. Emerg. Sel. Topics Power Electron.*, vol. 10, no. 6, pp. 7318–7332, Dec. 2022, doi: 10.1109/JESTPE.2022.3163051.
[58] T. Liu, Z. Zhou, A. Xiong, J. Zeng, and J. Ying, "A novel precise design method for LLC series resonant converter," in *Proc. INTELEC 28th Int. Telecommun. Energy Conf.*, Providence, RI, USA, Sep. 2006, pp. 1–6, doi: 10.1109/intlec.2006.251606.
[59] K. S. Sarath and S. Sekar, "An optimal design of LLC resonant converter using FireFly algorithm based parameter optimization approach," *J. Comput. Mech., Power Syst. Control*, vol. 2, no. 1, pp. 31–40, 2019.
[60] R. Zheng, B. Liu, and S. Duan, "Analysis and parameter optimization of start-up process for LLC resonant converter," *IEEE Trans. Power Electron.*, vol. 30, no. 12, pp. 7113–7122, Dec. 2015, doi: 10.1109/TPEL.2015.2389116.
[61] A. Lordoglu, M. O. Gulbahce, D. A. Kocabas, and S. Dusmez, "A holistic design optimization method for LLC converters in light electric vehicle chargers," *IEEE Trans. Transport. Electrific.*, early access, Jul. 24, 2023, doi: 10.1109/TTE.2023.3298170.
[62] Y. Ding, S. Gregov, O. Grodzevich, I. Halevy, Z. Kavazovic, O. Romanko, T. Seeman, R. Shioda, and F. Youbissi, "Discussions on normalization and other topics in multiobjective optimization," in *Proc. Fields-MITACS, Fields Ind. Problem Solving Workshop*, 2006, pp. 89–101.
[63] B. P. Flannery, *Numerical Recipes in C*, vol. 24. New York, NY, USA: Press Syndicate of the Univ. Cambridge, 1992, p. 78.
[64] D. Zaikin, *LLC Converter Design and Optimization (C Language Code)*. Figshare. Software, 2023. [Online]. Available: https://figshare.com/, doi: 10.6084/m9.figshare.22633423.

DENYS IGOROVYCH ZAIKIN (Member, IEEE) was born in Kharkiv, Ukraine, in 1976. He received the M.S. degree in radio-electronics engineering from Kharkiv National University of Radio Electronics, in 1999.

From 2002 to 2008, he was an Electronics Developer for microwave and radar systems with the Institute of Radio Astronomy, National Academy of Sciences of Ukraine. Since 2008, he has been with EKTOS-Ukraine LLC, Kharkiv, as a Power Electronics Developer and an EMC Specialist. From 2010 to 2014, he was a Power Electronics Developer with Danfoss Solar Inverters, Grasten, Denmark. He is currently a Senior Power Electronics Engineer with Advent Technologies A/S (former Serenergy A/S), Aalborg, Denmark. His research interests include switching mode power supply, converter modeling, magnetics, and EMC research.

MARTIN KOLDING ANDERSEN was born in Hobro, Denmark, in 1987. He received the B.Sc. and M.Sc. degrees in EE from Aalborg University, in 2010 and 2012, respectively. He joined the Faculty of Energy Technology, Aalborg University, as a Research Assistant. In 2013, he joined Advent Technologies A/S (former Serenergy A/S) as a Control and Software Engineer. He is currently a Senior Engineer, where he develops embedded software, control, and automation for HT PEM fuel cell systems. This includes everything from system design, advanced control, large data analysis, power converter SW, and everything else making the fuel cell autonomous.

MARK BRIX RUGTVED RUGHOLT was born in Frederikshavn, Denmark, in 1992. He received the M.Sc. degree in mechatronic control engineering from Aalborg University, in 2016. He joined Serenergy A/S (later acquired by Advent Technologies A/S) as a Systems Control Engineer. Later, he transitioned to mechanical system design. In 2021, he joined the Software Engineering Team, as a Software Control Engineer, where he developed the fuel cell mechatronic control structure and application state management for embedded systems.

THOMAS KRAG KJELDSEN was born in Aalborg, Denmark, in 1980. He received the M.Sc. degree in electrical engineering specializing in applied signal processing from Aalborg University, Denmark, in 2007. He joined Prevas A/S directly after university, working as an Embedded Software Consultant involved in several product development projects. In 2014, he joined RTX, Palo Alto, USA, working as a Field Application Engineer. In 2015, he returned to RTX headquarters, Aalborg, working first as a Project Engineer and later as a Project Manager. He joined Advent Technologies A/S, in 2022, where he is currently heading the System Control Team, with overall responsibility for both SW and HW development.

POOYA DAVARI (Senior Member, IEEE) received the B.Sc. and M.Sc. degrees in electronic engineering from the University of Mazandaran, Iran, in 2004 and 2008, respectively, and the Ph.D. degree in power electronics from QUT, Australia, in 2013.

From 2005 to 2010, he was involved in several electronics and power electronics projects as a Development Engineer. From 2013 to 2014, he was a Lecturer with QUT. He joined Aalborg University (AAU), in 2014, as a Postdoctoral Researcher, where he is currently an Associate Professor. He is also the Leader of the EMI/EMC in Power Electronics Research Group and the Vice Chair of the Energy Efficiency Mission, AAU Energy. He has been focusing on EMI, power quality, and harmonic mitigation analysis and control in power electronic systems. He has published more than 200 technical articles. He is a member of the Joint Working Group Six and Working Group Eight at the IEC Standardization TC77A. He was a recipient of the Equinor 2022 Prize (Denmark Oldest Engineering Award) and the 2020 IEEE EMC Society Young Professional Award for his contribution to EMI and harmonic mitigation and modeling in power electronic applications. He is the Founder and the Chair of the IEEE EMC Society Chapter Denmark. He served as the Guest Associate Editor for IEEE JOURNAL OF EMERGING AND SELECTED TOPICS IN POWER ELECTRONICS, *IET Power Electronics*, IEEE ACCESS, *Journal of Electronics*, and *Journal of Applied Sciences*. He is an Associate Editor of IEEE TRANSACTIONS ON POWER ELECTRONICS, IEEE TRANSACTIONS ON TRANSPORTATION ELECTRIFICATION, IEEE JOURNAL OF EMERGING AND SELECTED TOPICS IN POWER ELECTRONICS, *Journal of Power Electronics*, and *IET Electronics*, and an Editorial Board Member of *Journal of Applied Sciences* and *Journal of Magnetics*. He is the Editor-in-Chief of *Circuit World*.